Università degli Studi di Trieste

Facoltà di Scienze Matematiche, Fisiche e Naturali
Corso di laurea specialistica in Fisica

Tesi di laurea

Towards the observation of ultrafast demagnetization by high harmonic generated ultraviolet coherent pulses

Verso l'osservazione di fenomeni di demagnetizzazione ultraveloce con impulsi coerenti ultravioletti generati da armoniche superiori

Laureando:
Giulio Vampa

Relatore:
Ch.mo Prof. Fulvio Parmigiani

Correlatore:
Dott. Alberto Simoncig

Anno Accademico 2009 - 2010

A Mauro ed Annalisa

"L'ottimismo è il sale della vita!"
Barbara

Contents

Introduzione **1**

Introduction **5**

1 Setting the context:
"*the smaller, the faster*" **9**
1.1 State of the art of ultrafast magnetism 14

2 Introduction to Magnetic Dichroism **19**
2.1 Dichroism in absorption: the XMCD effect 19
2.2 Dichroism in scattering or reflection 22

3 High order Harmonic Generation **27**
3.1 Phenomenology of the HHG process 29
3.2 Comparison with other coherent EUV/SXR sources 33

4 Experimental apparatus **37**
4.1 The LASER source 37
4.2 The coherent ultrashort EUV source 38
4.3 The TR-EUV/MLD experimental chamber 40

5 Multilayer Optics **45**
5.1 Theory of multilayer optics 45
5.2 Characterization of multilayer spherical mirrors 48
5.3 Obtaining circular polarization with multilayers 51

6 Experimental data **53**
6.1 Static data 53
6.2 Towards ultrafast demagnetization dynamics 58

Conclusions **63**

A Derivation of reflection coefficients for T-MOKE **67**

List of Figures **71**

List of Acronyms **75**

List of Symbols **75**

Bibliography **77**

Ringraziamenti **83**

Introduzione

La nostra società dell'informazione esige in continuazione sempre maggiori spazi per l'immagazzinamento dei dati e uno scambio di bit sempre più veloce. Questa richiesta sta innescando la ricerca attuale in due aree differenti, ma molto correlate: da un lato c'è la ricerca verso bit magnetici più piccoli; dall'altro quella per velocità di lettura e scrittura dei loro contenuti più rapide.

Nonostante la sfida della miniaturizzazione fino alla scala nanometrica stia affrontando problemi fondamentali, molto può ancora essere fatto per migliorare i tempi di scrittura.

Alla fine degli anni '90 fu scoperta una dinamica di demagnetizzazione nel regime del picosecondo (10^{-12} s) [1] indotta da impulsi laser intensi della durata del femtosecondo (10^{-15} s). La ricerca attuale ha confermato questo comportamento in tutti i metalli di transizione 3d (Fe, Co, Ni) ed altri composti. L'interesse delle industrie *high-tech* si sta focalizzando su questo settore scientifico emergente, chiamato *"femtomagnetismo"*, e sta stimolando di conseguenza la ricerca sperimentale e teorica in questo campo. Come verrà esposto nei prossimi capitoli, solo una comprensione superficiale della fisica coinvolta è stata data e molte domande fondamentali sono ancora senza risposta.

Il lavoro che verrà presentato si pone in questo contesto. Questa tesi si propone di spianare la strada verso lo studio delle dinamiche di demagnetizzazione ultraveloce attraverso misure di dicroismo magnetico risolte in tempo, effettuate con impulsi laser coerenti ed ultracorti nell'Ultravioletto Estremo (EUV) prodotti da una sorgente di Generazione di armoniche di ordine superiore (HHG). L'energia dei fotoni è scelta risonante con le soglie d'assorbimento $M_{2,3}$ dei metalli Fe o Ni. Quindi, la sensibilità alla specie chimica è ottenuta nell'esperimento.

Al momento, in letteratura è presente un solo lavoro sperimentale simile che imp-

iega una sorgente HHG [2], il quale rappresenta la prima applicazione di impulsi HHG a studi risolti in tempo nel campo della ricerca in stato solido. In quel caso sono stati usati impulsi di radiazione ultracorti linearmente polarizzati. Al contrario, il *setup* sperimentale presentato in questo lavoro è adatto a lavorare anche con luce polarizzata circolarmente, superando la difficoltà intrinseca nella generazione di tali stati di polarizzazione con le sorgenti HHG. La realizzazione di misure risolte in tempo con fotoni polarizzati circolarmente permetterà di sondare indipendentemente le dinamiche di *build-up* dei momenti angolari orbitale e di spin sulla scala temporale del femtosecondo.

Ad oggi si segnala un solo lavoro sperimentale su questi temi compiuto con luce polarizzata circolarmente [3] sulla soglia d'assorbimento L_3 del Ni, molto recentemente esteso alla soglia L_2 [4]. Per questi esperimenti è stata usata una *slicing beamline*, invece di una sorgente HHG, e nei prossimi capitoli ne verrà fornito un confronto dettagliato.

Le caratteristiche chiave di sensibilità alla specie chimica e di capacità di distinguere le dinamiche del momento angolare orbitale da quelle di spin saranno alla portata anche dei nuovi *Free Electron Lasers* (FELs), i quali supereranno molti dei limiti delle sorgenti sopracitate. Si prevede che gli studi sulla demagnetizzazione ultraveloce fioriranno con la diffusione di queste strutture.

Sebbene l'obiettivo sia quello di effettuare studi risolti in tempo con fotoni polarizzati circolarmente, molti problemi devono essere risolti per compiere misure così complicate. Tali problematiche sono analizzate nel corso dei prossimi capitoli. In questa tesi, dunque, sono presentate solo misure di dicroismo magnetico statico ottenute con luce polarizzata linearmente.

Questo ambizioso esperimento è il risultato di una collaborazione internazionale tra il laboratorio T-Rex ad Elettra e il *Center for X-Ray Optics* (CXRO) del *Lawrence Berkeley National Laboratory* (LBNL), situato a Berkeley (USA).

La tesi è strutturata come segue.

- Nel capitolo 1 è descritto il contesto tecnologico, seguito da una rassegna della fenomenologia e della comprensione teorica conosciuti finora delle dinamiche di demagnetizzazione ultraveloce indotta da impulsi laser
- Nel capitolo 2 si descrive la tecnica utilizzata per ricostruire le proprietà magnetiche del campione studiato. Particolare cura è posta nella presentazione delle

caratteristiche principali proprie degli esperimenti compiuti nelle regioni spettrali dell'EUV o dei Raggi X, rispetto a quelli compiuti nella regione ottica.

- Nel capitolo 3 è esaminato il processo HHG ed è fatto un confronto con altre sorgenti EUV coerenti.
- Nel capitolo 4 è descritto tutto il *setup* sperimentale: dalla sorgente LASER a quella HHG, e la camera sperimentale.
- Nel capitolo 5 si dimostra come la luce EUV possa essere manipolata per mezzo di dispositivi ottici specificatamente sviluppati. Dopo una breve descrizione teorica dei principi sui quali si basano, si presenta la caratterizzazione degli specchi usati nell'esperimento. Attenzione è data alle loro proprietà di filtraggio della luce e a come queste influiscano sull'esperimento.
- Nel capitolo 6 si presentano i dati acquisiti, insieme ad una discussione dettagliata delle complicanze incontrate durante l'esperimento. I problemi che devono essere risolti per l'acquisizione di misure risolte in tempo sono evidenziati nell'ultima parte di questo capitolo

In ultimo saranno tratte le conclusioni.

Introduction

Our Information Society is continuously demanding for higher and higher data storage capacities and faster and faster exchange of bits. This request is triggering current research on two different, but very much correlated, areas: on one side there's the quest for smaller magnetic bits; on the other side the one for faster reading and writing of its content.

Even though the challenge to miniaturization to the nanoscale is facing fundamental problems, much can still be done to improve write timings.

At the end of 1990s it was discovered a demagnetization dynamics in the low picosecond (10^{-12} s) regime [1] induced by intense laser pulses with femtosecond (10^{-15} s) time duration. Current research has confirmed this behaviour to all 3d transition metals (Fe, Co, Ni) and other compounds. This emerging field of science, termed "*femtomagnetism",* is polarizing the interest of high-tech industries, boosting experimental and theoretical research in this field. As reviewed in the next chapters, only a shallow understanding of the physics involved has been given and many fundamental questions are still unanswered.

The work being presented here sets in this frame. This thesis aims at paving the way towards the study of ultrafast demagnetization dynamics by time-resolved magnetic dichroism, performed with coherent ultrashort Extreme Ultra-Violet (EUV) laser pulses delivered by a High order Harmonic Generation (HHG) source. The photon energy is chosen to be resonant with the $M_{2,3}$ absorption edges of Fe or Ni metals. Hence, the elemental sensitivity is achieved in the experiment.

At present, only one similar experimental work that employs an HHG source is reported in literature [2], providing the first application of HHG pulses to time-resolved studies in condensed matter research. In that case linearly polarized ultra-short-

radiation pulses are used. Conversely, the experimental setup presented here is suitable to work also with circularly polarized light, overcoming the intrinsic difficulty of generating such polarizations with HHG sources. Performing time-resolved measurements with circularly polarized photons will allow to independently probe build-up dynamics of the orbital and spin angular momenta on the femtosecond time-scale.

So far, only one experimental work on this topic was performed with circularly polarized light [3] at the L_3 absorption edge of Ni, very recently extended to the L_2 edge [4]. For these experiments a *slicing beamline* was employed, rather then an HHG source, and a critical comparison between these two techniques is given in the next chapters.

The key features of elemental sensitivity and distinction of spin and orbital angular momenta dynamics will be at the reach also of the new Free Electron Lasers (FELs), which will overcome many of the limitations of the aforementioned sources. Ultrafast demagnetization studies are expected to boom with the wide-spreading of these facilities.

Although the goal is performing time-resolved studies with circularly polarized photons, many issues have to be solved to carry out such complicated measurements and they are reviewed throughout the following chapters. Hence, in this thesis only static magnetic dichroism obtained with linearly polarized light is presented.

This challenging experiment is a result of an international collaboration between the T-ReX Laboratory at Elettra and the Center for X-Ray Optics (CXRO) of the Lawrence Berkeley National Laboratory (LBNL), located in Berkeley (USA).

The thesis is structured as follows.

- In chapter 1 the technological context is described, followed by a review on the phenomenology and theoretical understanding of laser induced ultrafast demagnetization dynamics known so far.

- In chapter 2 it is given a description of the technique employed to resolve the magnetic properties of the sample under study. Care is given in the presentation of the main features that experiments in the EUV or X-Ray spectral regions have with respect to those performed in the optical region.

- In chapter 3 the HHG process is briefly reviewed and a comparison with other coherent EUV sources is made.
- In chapter 4 the whole experimental apparatus is described: from the LASER to the HHG sources, and the experimental chamber.
- In chapter 5 it is shown how EUV light can be handled by means of specifically developed optical devices. After a brief theoretical description of their working principles, it is reported the characterization of the mirrors used in the experiment. Attention is given to their light filtering properties and how these affect the experiment.
- In chapter 6 the acquired data is presented, together with a detailed discussion on the issues encountered during the experiment. The problems that must be solved for acquisition of time-resolved measurements are highlighted in the last part of this chapter.

Conclusions are finally drawn.

Chapter 1

Setting the context:
"*the smaller, the faster*"

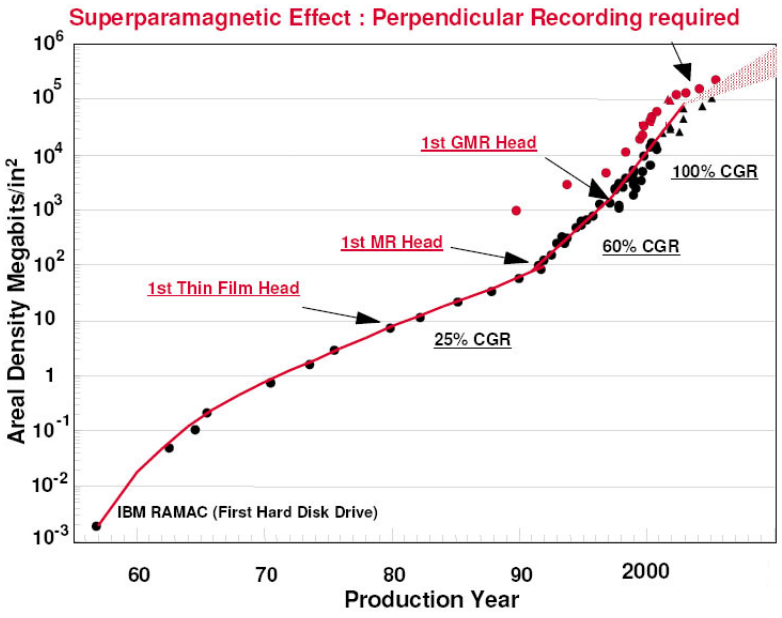


Figure 1.1: Areal density of commercial storage devices versus the year they came on the market.

Fig. 1.1 shows on a logarithmic scale the increase of areal density of previous hard drives versus the availability when these devices were on the market. The scaling trend is impressive: about a factor of 1000 in ten years. The human kind has hardly seen a comparable technological increase of performances ever. Present bit dimensions are

$\simeq 30 \times 190$ nm but high-tech industries are pushing to the limit of tens of atomic dimensions, i.e. few nanometers. But doing so, many fundamental problems arise.

When coming to nanometer grain sizes processes of *thermal self erasure* make it impossible to store the information in a bit for sufficiently enough time. This effect is explained in terms of the *super-paramagnetic limit*. In nanometer sized ferromagnets or ferrimagnets the stable magnetic moment of a single nanoparticle usually is aligned along a specific axis, called the "easy axis", and the orientation along this axis defines the information stored, either 0 or 1, up or down. To flip the orientation of a magnetic moment from "up" to "down" it must rotate out of the easy axis, i.e. through a hard plane. Since the stable configuration corresponds to magnetic moments directed along the easy axis, this rotation requires energy. The energy barrier that must be overcome is given by the product KV, where K is the magnetic anisotropy constant and V is the nanoparticle volume [5]. The *super-paramagnetic* state is encountered when the grain dimension is so small that thermal fluctuations, with energy k_bT, are enough to overcome this energy barrier and the magnetic moments start flipping, i.e. the information cannot be stored anymore. When the easy axis is in the longitudinal direction of the magnetic strip this effect limits the areal density to $\approx 100 \div 200$ Gbit/in^2, while when it is perpendicular to it the limit is relaxed to ≈ 1024 Gbit/in^2 and the grain size can be pushed down to $\approx$10 nm, really approaching the few atoms cluster per each nanoparticle, where magnetization must be controlled directly through spin degrees of freedom. The word "*spintronic*" was coined for this emerging branch of quantum control of the magnetic properties [5]. However, also with perpendicular recording the super-paramagnetic limit is still there. To keep the bit in place, a lot of research is currently trying to increase the anisotropy constant K by testing new materials, but then higher and higher fields or slower recording speeds (as in *heat assisted recording*) are needed to flip the magnetic moment [5]. How feasible can this solution be?

Although the race to miniaturization presents these fundamental issues, much can still be done on the writing speed side.

Indeed present technology limits the write speed to low GHz rates, that is each writing process takes ≈ 1 ns [5, 6]. It employs the so-called *Oersted switching* in which the magnetic moment is flip by a magnetic field in a two-step process*:* in the first step

the field induces a precession of the magnetic moment around the field axis and, in the second step, damping of the motion by transfer of energy and angular momentum to the underlying lattice fixes the magnetization in the new position. The precessional period is typically $\simeq 10$ ps at 1 T magnetic field, while damping is strongly dependent on many factors like the magnetic anisotropy and usually takes $100s$ ps. The overall process usually doesn't take longer than hundreds of ps. The origin of the ≈ 1 ns time-scale resides in the fact that no torque is exerted when the applied field is exactly anti-parallel to the actual magnetization orientation, so no switching is expected. But at room temperature the magnetic moment is not exactly fixed, it fluctuates around the average position, and a very small torque can be exerted that eventually, very slowly, flips it [5]. A better way can be used in which thermal heating starts the precessional motion, but then control on the damping is required to stop it in the right position [5]. Besides, the limit of hundreds of picoseconds is hardly overcome since the same physical effects are employed.

Tomorrow research is aiming at flipping the magnetic moment by applying a current pulse rather than a magnetic one. This effect, called *spin-torque effect*, is the reverse of the *giant magnetoresistance effect* (GMR), a pure quantum-mechanical phenomenon which is presently used in read heads. The GMR is a different resistivity of a material buried in two magnetic layers when the magnetization of one layer is parallel or anti-parallel to that of the other one. It states the ability to control a current through the magnetization, while the *spin-torque* effect is exactly the opposite: the ability to control the magnetization by applying a current to the bit.

Other interesting effects can be exploited to control the magnetization dynamics. For instance it can start with an excitation of the system by an intense ultrashort laser pulse (in the femtosecond regime, 10^{-15} s). Very recently higher frequency spin wave excitations up to 140 GHz were obtained by excitation of transient magnetic anisotropy fields [7, 8]. This anisotropy is induced by the temperature variation of the lattice provided by the laser pulse. Soon after, a magnetization dynamics at 400 GHz was reported that took advantage of the so-called *inverse Faraday effect* [9]. All these findings prove the ability of controlling the magnetization by means of laser pulses. However way faster magnetization dynamics obtained with laser pulses are under the spotlight of current research.

But what is the fastest achievable flipping?

Reducing the grain size also affects the writing speed limit. To keep a magnetic moment in place a balance of many energetic terms must be obeyed, as happens between exchange energy (that prefers parallel spins) and classical magnetic moment interaction (that prefers anti-parallel spins) in the microscopic domain formation. Each energy scale goes, hand by hand, with a length scale: higher energies are linked to shorter interaction distances, and conversely [6, 5]. Hence, smaller and smaller bit dimensions require higher and higher energies to hold it. Furthermore, the energy scale is intimately linked to a proper time scale by the single-cycle limit $t = h/E$, as shown in Fig. 1.2, where timescales for three typical magnetic energies are reported. Nanometer sized bits are approaching the energetic range of *exchange energy* which is of the order of 10^{-1} eV [6]. Exchange mediated processes happen in the femtosecond regime (THz frequency range), six orders of magnitude below the current write timing limit of ≈ 1 ns and at least two orders below the aforementioned laser induced dynamics.

Exciting new research on the interaction of intense femtosecond laser pulses with materials that leads to ultrafast magnetization dynamics in the THz range has just begun and the term *femtomagnetism* is already spreading in the scientific community. Industries are also strongly interested in this forefront research since *femtomagnetism* naturally satisfies world-leading brands slogan: "*the smaller, the faster*".

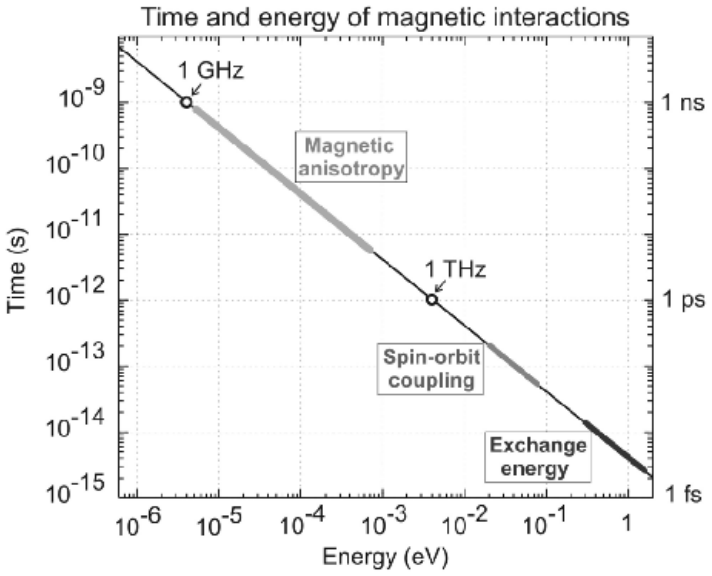


Figure 1.2: Time - energy correlation line given by $t = h/E$. The typical energetic ranges of magnetic interactions are also shown. (From [6])

In the next chapter the state-of-the-art of ultrafast magnetization dynamics is presented.

1.1 State of the art of ultrafast magnetism

The first work that evidenced a modification of the magnetic state of a system under the influence of an intense short laser pulse is due to Agranat *et al.* [10]. They reported a demagnetization of a ferromagnetic Ni film using 10s ps and 40 ns laser pulses, concluding that the characteristic time-scale is in the nanosecond regime. Subsequently Vaterlaus *et al.* [11, 12] showed that the demagnetization time can be as fast as $\simeq$ 100 ps in Gd and from 30 ps to 20 ns in Fe.

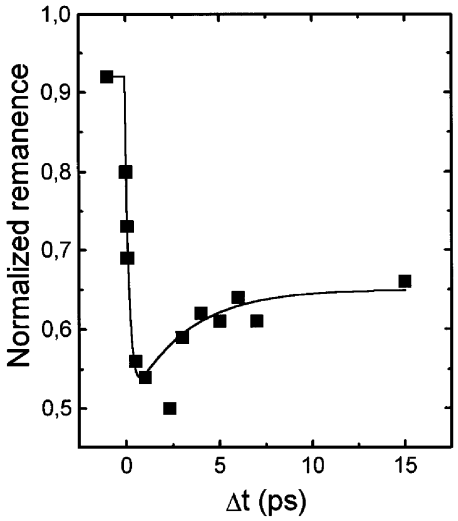


Figure 1.3: Experimental result of Beaurepaire. The trace is proportional to the sample magnetization. Soon after the *pump* pulse excites the system, the magnetization drops, evidencing a $\simeq$ 2 ps demagnetization dynamics. (From [1])

A surprising effect was discovered by Beaurepaire *et al.* [1] in 1996, who showed a magnetization loss in few picoseconds (Fig. 1.3), orders of magnitude less than previously reported and out of any theoretical understanding. In their work they studied a Ni thin film with a *pump-probe* technique: first an intense laser pulse excites the system, then a second less intense pulse, delayed in time with respect to the first, probes the transient state without sensibly modifying it. The time resolution employed in their experiment was about 60 fs. The result of Beaurepaire triggered a lot of interest in the scientific community opening the new era of *femtomagnetism.*

Subsequent research [13, 14, 15] evidenced the presence of another ultrafast dynamics that precedes the one on the picosecond time-scale: this demagnetization takes

place within the first ≈100 fs hence within the *pump* pulse duration. Since it is driven by the laser pulse it is also referred to as "coherent" dynamics, whereas the subsequent demagnetization is termed "incoherent".

A phenomenological model termed "three temperature model" (3TM) [1] was adopted to account for the experimental findings. It is an extension of the widely used "two temperature model" (2TM) [16] that describes energy transfer in a condense matter system between the various relaxation channels after excitation by an ultra-short laser pulse.

In the 2TM the amount of energy stored by the physical system is conveniently split in two separate energy *reservoirs*, or *baths*: one for the electrons and one for the lattice. They are thought in thermal equilibrium so the energy content and the capacity of each bath are described by a temperature and a thermal capacity. The justification of this artifact is that electromagnetic radiation couples preferentially with electron charges so that in the interaction of the system with the laser pulse, energy is deposited only in the electron bath, leaving the energy content of the lattice unchanged.

During the interaction with the laser field a collective electronic oscillation is induced that is in phase with it, i.e. it is *coherent*. When the field turns off the collective motion is destroyed within $\lesssim 10$ fs by phase destructive events (*incoherent* processes) like electron-electron, electron-phonon and electron-defects scattering. These processes are elastic, so the initial energy deposited by the laser field is redistributed within the electron bath and generates a non-thermal (non Fermi-Dirac) energy distribution. In the subsequent ≈ 100 fs electron thermalization occurs by inelastic electron-electron scattering and this bath reaches temperatures as high as 1000 K, in virtue of its small heat capacity. Since the lattice temperature is still unchanged, a high non-equilibrium state exists between the two *reservoirs*. Thus, according to the 2TM, energy flows from the electrons to the lattice by electron-phonon coupling and complete thermalization of the system typically occurs in some picoseconds (in metals).

In ultrafast demagnetization processes, conservation of angular momentum dictates that a transfer of spin angular momentum to another *reservoir* must occur. Hence a new relaxation channel must be considered that accounts for either exchange of energy and angular momentum.

This is done in the 3TM by introducing a *spin-wave* or *magnon* bath that couples

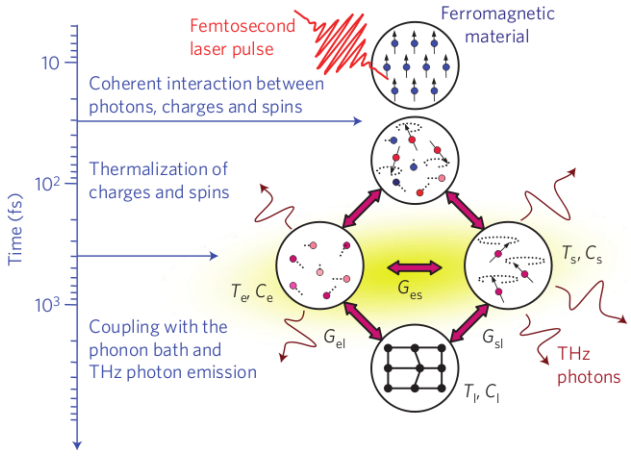


Figure 1.4: Representation of the ultrafast demagnetization process. A femtosecond laser pulse interacts *coherently* with charges and spins of electrons, which subsequently thermalize and interact together with the lattice (*incoherent* evolution). The relative weight of the deexcitation channels and the nature of the relaxation process is highly debated. The demagnetization is also found to emit THz photons [17]. (From [15])

to either the electron and lattice *reservoirs*. Transfer of energy and angular momentum occurs via spin-flip events that change the magnetic moment along the quantization axis [16].

Beaureparie *et al.* could simulate the experimental behaviour by means of this model, even though the relative weight of the various relaxation channels and the microscopic understanding of the transfer of angular momentum between the *reservoirs* is still a highly debated topic. A pictorial representation of all the mentioned steps is given in Fig. 1.4.

By now the same experimental behaviour is confirmed with many different experimental techniques for all elementary ferromagnetic transition metals (Co, Ni, Fe) and several alloys thereof [18].

Insight into the microscopic nature of the *coherent* demagnetization, that happens within the laser pulse, is provided by Bigot *et al.* [15]. Since in linear light-matter interactions the radiation field doesn't couple with the spin degree of freedom, they suggest that the observed coupling has its origins in non-linear relativistic quantum

electrodynamics through the terms:

$$\begin{aligned} &\text{Term (a):} \quad -\tfrac{e\hbar}{2m}\vec{\sigma}\cdot\left[\vec{B}(\vec{r},t)+\tfrac{1}{2mc^2}\vec{E}(\vec{r},t)\vec{p}\right] \\ &\text{Term (b):} \quad -i\tfrac{e\hbar}{8m^2c^2}\vec{\sigma}\vec{\nabla}\times\vec{E} \end{aligned}$$

They argue that these terms become relevant in the presence of the intense ultrashort laser pulse since the magnetic field $\vec{B}$ can reach intensities up to 1 T, and the atomic potential is also modified by the laser electric field $\vec{E}$. As a result they expect the spin dynamics to be affected by these dynamical terms, although no calculations have been performed yet.

The nature of the subsequent *incoherent* dynamics on the other hand is controversial. In this temporal regime thermalization of electron, spin and lattice populations take place, i.e. exchange of energy and angular momentum occurs among these *baths.* At present, however, it is hard to say if spins preferentially interact with the electrons or the lattice. Furthermore, the microscopic nature of this interaction is completely unknown. For example Zhang and Hübner [19] suggest that demagnetization proceeds through coupling of spin and angular momentum, without including the lattice degree of freedom. On the other hand Stamm *et al.* [3] showed that the electron orbits do not act as a *reservoir* of angular momentum, leaving only dissipation of it to the lattice as a viable channel. As proposed by Koopmans *et al.* [18], this phonon or impurity mediated deexcitation channel can be modeled in terms of a spin-dependent Elliot-Yafet type of scattering. This process is able to calculate the probability of a spin-flip event on emission or absorption of a phonon. Although the model can describe on the same foot the ≈ 1 ps incoherent dynamics and the longer $100s$ ps one, Bigot *et al.* complain that there are many experimental evidences in disfavor of this hypothesis. According to them the spin-phonon scattering cannot describe, for instance, the different electron and spin thermalization times [15].

In conclusion ultrafast demagnetization studies are really forefront research as many fundamental questions are still unanswered. The main doubts concern the transfer of angular momentum among the different *baths.* What are the main deexcitation channels? According to recent measurements a coupling of the spin *reservoir* to the lattice seems to be favored, although also other channels were proved to be active.

Furthermore the microscopic origin of it is highly controversial. In particular a spin-dependent scattering between electrons and lattice can explain some basic dynamics but, at present, is not proved to describe other aspects of the process.

The *coherent* demagnetization that takes place within the laser pulse is also under the spotlight. A direct photon-spin interaction has been introduced to explain it, and it may be interesting to understand how it acts on the subsequent free demagnetization. For example, is it possible to short the thermalization times by properly modifying the *coherent* dynamics? A question of capital importance for technological advance.

Current research on this topic is willing to answer all these questions as the present understanding of the physics involved is completely unsatisfactory.

Chapter 2

Introduction to Magnetic Dichroism

This chapter reports a brief description of the magnetic properties of matter and optical magnetic dichroism. Two experimental techniques that are capable of measuring this effect are reviewed and particular care is addressed in a comparison of the two. In the last paragraph it is given the main reason that explains the choice of one technique with respect to the other for the current experiment.

2.1 Dichroism in absorption: the XMCD effect

In the interaction of electromagnetic radiation with materials the term "dichroism" is referred to a dependence of absorption on the polarization of light [6]. This term refers to the fact that when these materials are shone with white light they appear of two (*di-*) different colors (*chroma*) for two different light polarizations.

Magnetic Dichroism arises when materials present some kind of magnetic ordering and it depends on the electrons spin and charge distributions in the valence band. This effect is highly enhanced when light in the Extreme Ultra-Violet (EUV) or X-Ray region of the spectrum is employed, for the presence of absorption resonances of higher cross section, like those involving electronic transitions from occupied core states to empty valence band states (above the Fermi energy).

X-Ray Absorption Spectroscopy (XAS) is a powerful tool to study electronic and magnetic properties of such empty states [6]. In XAS each spectral line identifies an allowed electronic transition. As stated by *sum rules* [6], the integral of the measured

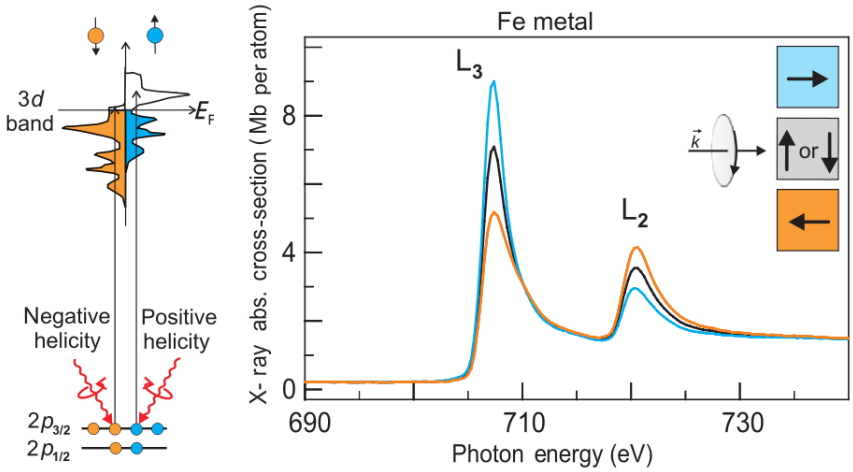


Figure 2.1: The XMCD effect at the $L_{2,3}$ edges of Fe. (right) XAS spectra obtained with circular polarization at different magnetization orientations (showed as arrows in the colored boxes). (left) Pictorial representation of the spin-dependent absorption process. The core states are assumed spin-orbit split, while the valence band is spin-split (From [6]).

absorption cross section (the spectral line intensity) is directly proportional to the total number of valence holes in the electronic ground state[1], integrating out all spin degrees of freedom. The key feature of magnetic dichroism is that the absorption process is made spin dependent. In particular, by means of circularly polarized light (X-Ray Magnetic Circular Dichroism - XMCD), the dichroic signal becomes directly proportional to the difference between spin-up and spin-down holes density of states[2] and so gives a straightforward determination of the net atomic magnetic moment, i.e. its magnetic properties [6].

Fig. 2.1 shows XAS spectra across the Fe $L_{2,3}$ absorption edges, which are split by spin-orbit interaction, for different orientations of the sample magnetization. The X-Rays are circularly polarized. A different intensity is recorded when the magnetization is rotated. The same effect can equivalently be observed changing the helicity of the light at fixed magnetization orientation [6]. The maximum XMCD effect is obtained

[1]This is valid after proper averaging of the spectrum over three orthogonal orientations of the crystal with fixed light polarization or over three polarizations (linear, left circular, right circular) at fixed crystal orientation. The rule is valid for $2p \rightarrow 3d$ (L-edge) transitions [6]. Extension to other transitions is not straightforward as some assumptions made for its derivation may not be fulfilled for other cases.

[2]Or equivalently of spin-up and spin-down electrons density of states

for parallel orientations of the magnetic moment $\mathbf{m}$ and the photon angular momentum $\mathbf{L_{ph}}$[3], while no effect is present when they are orthogonally oriented.

To observe *magnetic* dichroism two conditions must be often met: (i) the presence of a net magnetic moment of the valence band and (ii) spin-orbit split core states[4]. Formal calculations of the different absorption intensities take advantage of tabulated transition matrix elements between such states and an example is given in [6]. However a more intuitive pictorial representation of the process is available and is termed "*two-step* model" [6] (sketched in Fig. 2.1).

To describe the model a very simple case is considered in which the valence band doesn't carry any net angular momentum, but just a spin magnetic moment.

In the first step absorption of the photon transfers its angular momentum to the core electron, as allowed by dipole selection rules. If the photoelectron originates from a spin-orbit split level, then the angular momentum of the photon can be partially transferred to the photoelectron spin, which becomes spin-polarized with the quantization axis directed along that of the photon angular momentum. Since spin-flip transitions are forbidden by dipole selection rules, spin-up (spin-down) photoelectrons can only be excited to spin-up (spin-down) valence band hole states. The spin polarization is opposite for opposite photon helicities, and the ability of choosing it is at the core of the XMCD effect. It is also opposite for the two L edges due to the fact that the spin-orbit interaction is opposite. Indeed dichroic signals are reversed for the two edges, as shown in Fig. 2.1.

In the second step the spin-split valence band acts as a detector for the spin polarized photoelectrons and the transition probability is proportional to the empty electronic density of states of a given spin. Optimum "detection" occurs when the valence band quantization axis (the sample magnetization axis) is aligned with the photoelectron spin. In a non-magnetic material there's no net magnetic moment, hence both bands (spin-up and spin-down) contribute equally and the dichroism vanishes. Finally it easily understood how a dichroic signal can be measured reverting the magnetization

[3]Circularly polarized light can be thought of carrying an angular momentum of $l = 1$ directed along the k-vector. Left Circularly Polarized light carries an axial angular momentum equal to $q = +1$, while Right Circularly Polarized light has $q = -1$.

[4]A special case is that of $K - shell$ dichroism [6], in which the core states cannot be spin-orbit split. However, magnetic dichroism can still be observed if the valence band has a net orbital moment, that is if its empty density of states is imbalanced between upper and lower axial angular momentum.

at fixed polarization: when the magnetic field changes sign, so does the interaction that splits the valence band and spin-up and spin-down density of states exchange.

Summarizing, the XMCD intensity is proportional to [6]:

$$I_{XMCD} \propto \boldsymbol{m} \cdot \mathbf{L_{ph}} \propto < m > \cos\theta.$$

A characteristic of the XMCD effect is that it is linear in $\mathbf{m}$, making it particularly effective for study ferromagnetic or ferrimagnetic orderings, whereas it cannot be used in anti-ferromagnetic materials where the anti-parallel orientation of spins averages the dichroic signal to zero. Linearly polarized X-Rays (XMLD) must be employed in this case [6].

In common materials the valence band does carry a net orbital angular momentum and a dichroic signal can be present even in demagnetized states [6]. Hence, in magnetic materials the total effect will include both spin and angular momentum asymmetries of the density of states. However by properly averaging the magnetic dichroism over crystal orientations it is possible to quantify the spin magnetic moment m_s and the orbital magnetic moment m_o in an independent way, giving a unique description of its magnetic properties [6]. This is the characteristic that makes XMCD measurements so appealing.

Another characteristic of the measurements performed in the EUV or X-Ray spectral region, when compared to those performed in the optical of infrared region, is the *elemental sensitivity.* This is assured by the fact that only photons with an energy resonant with an absorption edge are detected by the sample. Hence this gives the possibility to study element specific properties in complicated materials like alloys or layered structures.

2.2 Dichroism in scattering or reflection

Magnetic effects are not limited to just different absorptions though: indeed in a classical phenomenological framework both the real and imaginary part of the refractive index become polarization dependent, only the latter being directly linked to absorption.

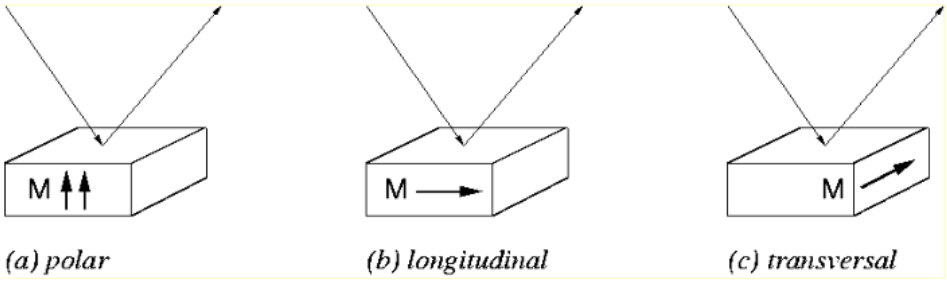


Figure 2.2: Three different geometries for the Kerr effect: (a) Polar geometry or P-MOKE, (b) Longitudinal geometry or L-MOKE and (c) Transverse geometry or T-MOKE. (From [20])

Hence, such effects are present also in scattering [21] and reflectivity experiments [22, 23, 1], the discovery of the latter *in the optical region* of the electromagnetic spectrum dating back the year 1876 by Rev. John Kerr (after whom the effect was called "Kerr effect")[5]. As like as XMCD however, considerably larger magnetic responses are obtained when X-Rays or EUV radiation resonant to atomic transitions are employed, giving this technique a high elemental sensitivity [23]. As a matter of fact, "resonant reflectivity" dichroic signals were reported to exceed those observed in XMCD experiments [24].

The Magneto-Optical Kerr Effect (MOKE) [20] is a rotation of the plane of polarization of linearly polarized light reflected off a material magnetized in the plane of reflection (either normal or parallel to the surface, see Fig. 2.2a-b). The reflected light appears also elliptically polarized[6]. When the magnetization of the sample is transverse to the plane of reflection (T-MOKE, see Fig. 2.2c) only a different reflectivity is seen when the polarization is in the plane of reflection (p-polarization), i.e. no rotation or ellipticity is induced[7]. No effect is encountered with polarization orthogonal to the plane of reflection (s-polarization). Hence, in T-MOKE, only an intensity measurement is required.

[5]As a matter of fact magneto-optical effects in the optical region of the electromagnetic spectrum were discovered well before quantum mechanics birth.

[6]This discovery is actually due to Righi in 1886 [20].

[7]This effect, which is termed "Transverse MOKE effect", was discovered by Zeeman in 1896 [20].

With this geometry, the reflection matrix takes the form [23][8]:

$$r_T = \begin{pmatrix} r_{ss} & 0 \\ 0 & r_{pp} \pm \Delta_{pp} \end{pmatrix}$$

where $|r_{ss}|^2$ and $|r_{pp}|^2$ are the non-magnetic Fresnel reflectance coefficients for respectively s- and p- polarized incident light. The $\pm$ sign refers to two anti-parallel magnetization orientations, and highlights the linear dependence of MOKE on $\mathbf{m}$ [20, 25]. This analogy between XMCD and MOKE reflects the fact that they are two faces of the same coin: they are two methods for measuring the same physical characteristics[9].

The magnetic contributions are enclosed in the complex term Δ_{pp}, which can be reconstructed from the total reflectivity of p-polarized light

$$R_\pm = |r_{pp} \pm \Delta_{pp}|^2 = |r_{pp}|^2 + |\Delta_{pp}|^2 \pm 2 \,\mathrm{Re}\left\{r_{pp}\Delta_{pp}^*\right\}$$

as [23]:

$$|\Delta_{pp}|^2 = \tfrac{1}{2}\left(R_+ + R_-\right) - |r_{pp}|^2$$
$$\mathrm{Re}\left\{r_{pp}\Delta_{pp}^*\right\} = \tfrac{1}{4}\left(R_+ - R_-\right)$$

As reported in appendix A, the reflection coefficients are obtained with Fresnel-Maxwell equations starting from a non-diagonal dielectric tensor (strictly connected to the complex refractive index) [20], where the off-diagonal terms are non-zero only for magnetic materials and are directly related to Δ_{pp}. Hence, complete knowledge on Δ_{pp} gives complete information of the variation of the refractive index due to magnetization.

Although with this treatment dielectric optical properties are easily related to measurable quantities such as intensities or polarizations, the drawback is that, alike in absorption experiments, MOKE dichroic signals are a mixture of the effects of both real and imaginary part of the dielectric tensor, and extracting information on spin and orbital moments is not straightforward [22]. Understanding the physics behind

[8]The reflection matrix (2×2) multiplied by the incident polarization vector (2×1) gives the reflected polarization vector (2×1). The entries of the polarization vector are the intensity and phase of the s- and p- components.

[9]However reflectivity measurements are more complete than absorption measurements, since they carry information on both real and imaginary part of the refractive index. The linear dependence on $\mathbf{m}$ brings MOKE near XMCD rather than XMLD (which is quadratic in $\mathbf{m}$), even though linearly polarized light is used [25].

the refractive index requires a quanto-mechanical treatment which is able to calculate the off-diagonal part of the dielectric tensor [20, 25] and predict reflectivity measurements from assumed density of states. Another way to understand the data can take advantage of the *atomic magnetic scattering factors* [6, 26], equivalent to the refractive index, underlining the close relation between scattering and reflectivity experiments [27, 28].

In this work resonant reflectivity measurements at the $M_{2,3}$ edges of Fe and Ni metals are performed, with the sample magnetic moment transverse to the plane of reflection. In this way no polarization analysis is required. The choice was made because of the low efficiency of polarizers in the EUV spectral region, that would not be enough to assure good photon flux on the detector with the employed EUV source. The overall efficiency of the HHG source and of each optic used in the experiment is being described in detail in the next chapters.

Even if only static magnetic dichroism data is presented in this thesis, in the near future, when time resolution is being implemented, the experiment will allow to probe build-up dynamics of both the angular and spin degrees of freedom and eventually separate their contribution to the signal by means of circularly polarized light.

Chapter 3

High order Harmonic Generation

In this chapter a brief review of the physics involved in High order Harmonic Generation (HHG) is given. These processes are able to produce Extreme Ultra-Violet (EUV) and Soft X-Rays (SXR) radiation from the interaction of strong ultrashort laser pulses with matter, like noble gases [29], molecules [30, 31] or surfaces [32].

The output pulses inherits the temporal coherence of the source having a duration from femtoseconds to hundreds of attoseconds.

As an example Fig. 3.1 shows a typical HHG emission spectrum obtained from the interaction between a $\simeq$ 50 fs laser pulse at $\simeq$ 800 nm with $\simeq$ 2.2 mJ and Ne (blue) and Ar (red). As it is possible to note only the odd harmonics of the fundamental radiation are produced.

The non-linear nature of the interaction, due to the short duration of laser pulses ($10 \div 60$ fs) and the high intensities of the electromagnetic field in the focus ($\approx 10^{15}$ W/cm^2), is witnessed by the breaking of the intensity scaling law typical of low order harmonics and the appearance of a "*plateau*" region in which the intensity is approximately constant, followed by a "*cut-off*" region, in which the emission abruptly falls down vanishing towards the maximum frequencies converted by the process.

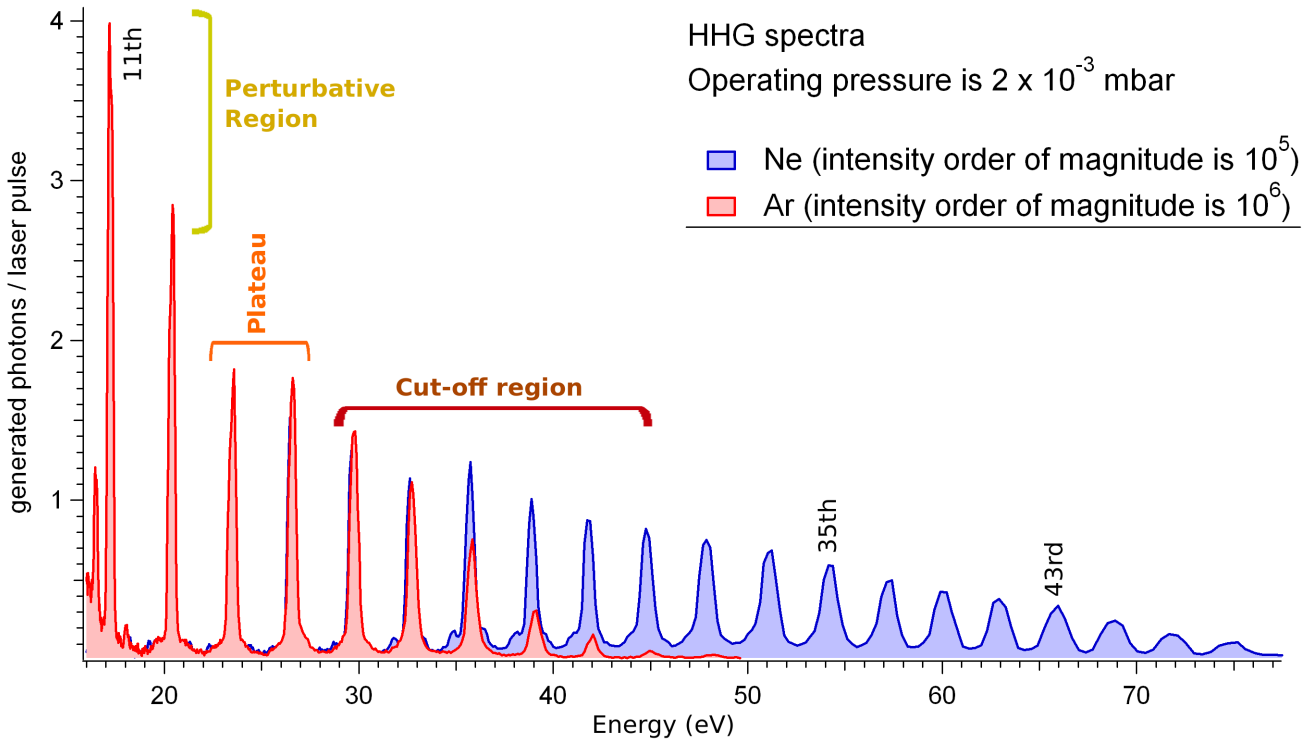


Figure 3.1: HHG spectra generated in Argon and Neon using $\simeq 2.2$ mJ, $\simeq 50$ fs, near-IR ($\lambda_0 \simeq 800$ nm) laser pulses. For Argon the perturbative, plateau and cut-off regions are highlighted. Due to the higher ionization potential I_p of Neon, its cut-off region extends to higher energy but the total number of photons is lower (this spectrum is multiplied by a factor of 10 in order to make a visual comparison with Argon). The 35th and the 43rd harmonics, employed in this thesis work, are resonant with respectively the Fe and Ni M-absorption edges.

3.1 Phenomenology of the HHG process

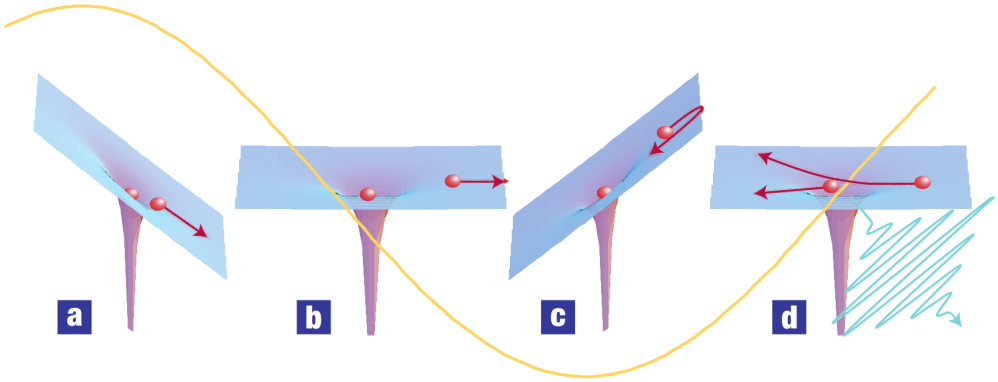


Figure 3.2: Pictorial representation of the HHG process. (a) the atomic coulomb barrier is lowered by the superposition with the oscillating laser field (yellow) allowing the electron leaving the atom by tunnel effect (ionization); (b) the same electron is driven away from the parent ion by the field and when this reverses (c) the electron is pulled back eventually colliding with the parent atom (d) while high order non-linear emission of photons can occur. (From [33])

The process can be described by a semiclassical model reported as "*three step model*" [34]. In the first step a bound electron is driven in a non-perturbative mode by the intense laser field and eventually ionizing the atom, in the second step the electron undergoes an oscillating motion imposed by the laser field and eventually colliding back with the parent ion in the third step. Fig. 3.2 shows a pictorial representation of the HHG process. Nonetheless, an accurate quantitative description must account for quantum effects, and a fully quantum model has been developed by Lewenstein and co-workers [35]. In the following the *three-step* model is briefly summarized.

Step 1: tunnel ionization

The interaction of a laser field, whose magnitude is comparable or stronger than the coulomb field of the atom, requires a quanto-mechanical treatment capable of predicting the ionization mechanism while quantifying the ionization rate of the atom [36].

The ionization mechanism is identified by the Keldysh's parameter $\gamma = \omega_0 \tau_T$, where ω_0 is the laser central frequency and τ_T is the tunneling time[1]. When $\gamma \gg 1$ the

[1]The tunneling time depends on the first ionization potential I_p and on the field peak amplitude

ionization is modeled via a multi-photon absorption process that promotes the bound electron to the continuum, whereas when $\gamma \ll 1$ ionization occurs by tunneling of the electron through the coulomb potential which is suppressed by the superposition with the laser field (Fig. 3.2(a)). In this regime the tunneling time τ_T at the field maximum, which is less than 200 attoseconds, is much shorter than the laser central frequency period ($T_{osc} \simeq 2.7$ fs) and the electron feels a static barrier.

The electron wavepacket becomes a coherent superposition of the initial bound state with a set of continuum states representing the ionized electron. As reported in [37], for near infrared laser radiation electrons are most probably tunneled during 300 attoseconds around each field crest near the pulse peak.

Step 2: wiggling in the laser field

In the second step the strong laser field dominates the motion of the continuum part of the electron wavefunction. Even though a quantum description is available [35], the motion in the direction of the field can be described in a classical framework because of the high number of photons interacting with the freed electron [33].

Electrons which are responsible for the emission of high order harmonics photons follow oscillating trajectories (Figs. 3.2(b-d)). The maximum distance the electron can travel is typically of the order of few nanometers, which is much larger than the atomic radius, therefore justifying treating the electron as a free moving particle in the laser field [38].

The time intercurring between the ionization and the collision back along with the acquired kinetic energy strongly depend upon the time the electron appears in the continuum (time-of-birth) [38]. The electrons that start the process before $T_{osc}/20$ following the electric field peak re-encounter the parent ion after $2/3T_{osc}$ and the trajectories are referred to as "*long paths*", while those starting after $T_{osc}/20$ re-collide before $2/3T_{osc}$ and the trajectories are referred to as "*short paths*".

Because of this behaviour, the harmonic emission takes place only each half cycle of the fundamental radiation, therefore, the Fourier transform from the time domain to the frequency domain will be giving harmonic emissions separated by $2\pi/(T/2) = 2\omega_0$. Hence, only odd harmonics of the fundamental will be generated.

The kinetic energy acquired by the electrons in the laser field has a maximum

E_0 as $\tau_T = \sqrt{2I_p}/E_0$[36]

around $T_{osc}/20$ and it is proportional to the amplitude of the electric field and to the square of the laser central wavelength. The maximum kinetic energy determines the maximum photon energy generated by the process, i.e. the "*cut-off*".

Even though the classical description gives very accurate predictions of the process (for instance, the estimate on the cut-off energy is only slightly modified by the quantum model), a quantum effect worth of note is represented by the spreading of the electron wavepacket in the direction perpendicular to the laser polarization [35, 31], as a direct consequence of the indeterminacy of the lateral momentum.

This effect expands the wavepacket with a gaussian profile at a velocity of $\simeq 5$ Å/fs, so that its full width at half maximum (FWHM) is $\simeq 5 \div 10$ Å at the moment of re-collision while the probability density at the parent ion is lower [33]. For the plateau harmonics this effect lowers the harmonic intensity of an order of magnitude using 800 nm laser radiation, compared to 400 nm laser radiation [39]. Nonetheless, the current density seen by the atom is very high, reaching values of the order of 10^{11} A cm^{-2} which is several orders of magnitude larger than conventional electron sources [33].

Step 3: electron re-collision

While re-encountering the parent ion, the bound state part of the wavefunction interferes with the continuum states wavepacket that propagates, producing a time dependent dipole that emits light [31], as shown in Fig. 3.3.

The wavelength of the emitted photon is related to the electron kinetic energy by the instantaneous frequency of the oscillating dipole, $\omega = E_{kin}/\hbar$. The spectral intensity and the phase of the harmonics are given by the Fourier transform of the

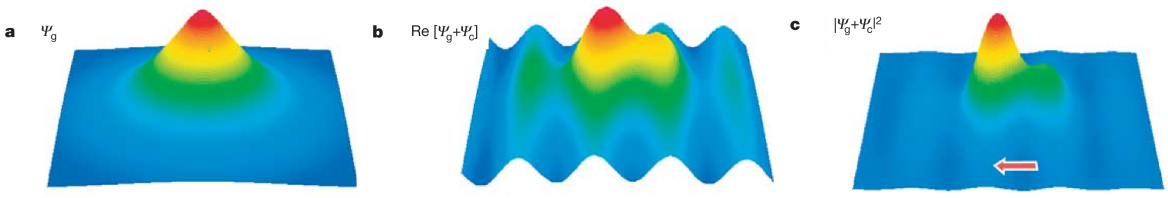


Figure 3.3: Illustration of the re-collision process: when the bound state electron wavefunction Ψ_g (a) is superimposed to the continuum wavepacket Ψ_c (b, that shows the real part) a dipole is induced (c), represented by an asymmetric charge density distribution. The induced dipole oscillates back and forth as the continuum wavepacket propagates, leading to emission of harmonics. (From [31])

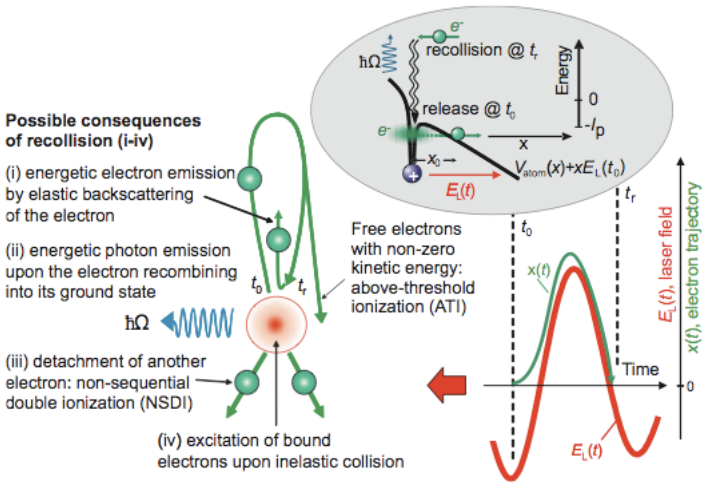


Figure 3.4: Processes that compete with the harmonic emission during the re-collision step. (From [40])

dipole acceleration spectrum, which can be related to the dipole moment

$$d(t) =< \Psi(t)| - e\boldsymbol{r}|\Psi(t) >$$

However, the emission of HHG radiation is not the only effect of the electron-ion collision. Other competing processes occur [34], as shown in Fig. 3.4: (i) the electron can be elastically scattered by the ion,acquiring a phase shift with respect to the laser field that leads to energy absorption and eventually high energetic electron emission; (iii) if the electron has enough kinetic energy it can promote another electron in the continuum (non-sequential double ionization); (iv) the electron can also inelastically scatter, leaving the ion in an excited state.

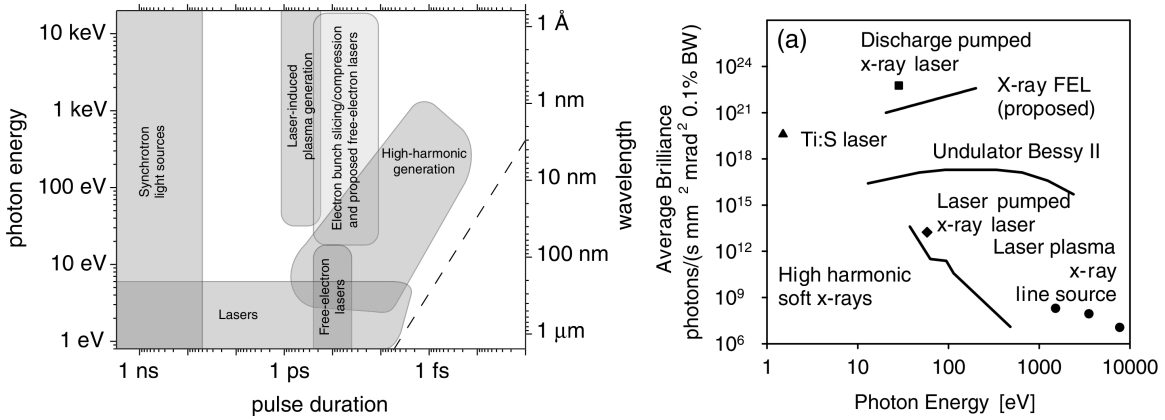


Figure 3.5: Comparison of present coherent EUV/SXR sources. On the left are plotted the regions of photon energy/wavelength and pulse duration that they cover. Ultrafast sources occupy the region not spanned by either synchrotrons or usual lasers. The dashed line represent the single-cycle limit. HHG sources can be very ductile and can produce pulses that are closest to this limit. (From [38]). On the right the average brilliance of these sources is shown. The most brilliant are FELs presently under construction, which have high peak brilliance and high repetition rate. HHG sources mainly suffer the low repetition rate, as explained in the text. (From [38])

3.2 Comparison with other coherent EUV/SXR sources

The production of ultrashort EUV and SXR light pulses has been a major breakthrough for studying the ultrashort (fs-as) time scales in a broad range of systems. The development of these sources is not yet ended, on the contrary, it is just dawning as witnessed by the several facilities that are spreading throughout the world.

Many complementary techniques have been employed at present and it is worth comparing High order Harmonic Generation with (i) electron bunch slicing/compression, (ii) free electron lasers (FELs) and (iii) laser-induced plasma.

As seen in Fig. 3.5 all these techniques can produce high energy and ultrashort light pulses, filling the region bordered by synchrotron facilities and laser systems. This fact has a deep explanation considering that the new sources take advantage of the high temporal resolution proper of lasers and the high energy of accelerated electrons proper of synchrotrons, mixing the core features of these "long-standing" sources.

In laser-induced plasma sources [38] X-ray generation is provided through "bremsstrahlung emission" by a hot electron plasma generated by the interaction between a very intense

femtosecond laser pulse and a high-density target (the "inverse bremsstrahlung absorption"). Since the plasma cooling down takes place in the sub-picosecond regime, X-ray pulses in the femtosecond regime are generated. Furthermore, after the interaction the generating laser pulse remains available as a *pump* pulse for time-resolved measurements.

However, some critical issues affect these sources, since they lack spatial coherence, having no directionality (the emission is isotropic), while high power lasers must be employed, limiting for the present days technology the repetition rate. The consequences are a low averaged flux and a low brilliance source, as shown if Fig. 3.5.

In electron bunch slicing [38] the interaction in an undulator of a femtosecond laser pulse with the several picosecond long electron bunch delivered by the synchrotron forms two femtosecond electron sub-pulses in the main bunch (two "slices") of lower and higher energy, respectively. These slices can be extracted from the bunch in the passage through a bending magnet generating a highly coherent X-ray beam in another undulator device (the "radiator").

Since only a small portion of the bunch is used, these sources are mainly limited by the low photon flux (close to 10 photons / laser pulse on the sample). Besides, a *pump* beam must be provided externally. Even so, the slicing technique has some advantages: the beam has a good spatial coherence and by means of a helical undulator a complete polarization control can be achieved [3]. This is of course an appealing feature for magnetic dynamics studies.

The low flux issue could be solved with the electron bunch compression [38], which can be obtained operating on the electron bunch with a magnetic chicane. In the magnetic chicane the slower electrons travel shorter paths with respect to faster electrons and bunch compression down to sub-picoseconds can be achieved.

In FELs [38] a compressed electron bunch is further microbunched in an undulator (the "modulator") by the interaction either with the radiation produced by the bunch itself (Self Amplified Spontaneous Emission, SASE) or with a *seed* laser (*seeded*-FEL). During propagation of the microbunch in another undulator (the "radiator") the radiation produced at each period adds coherently, producing very intense and highly brilliant X-ray beams, with excellent spatial coherence and a complete polarization

control. The duration of FEL pulses is typically in the $10 \div 500$ fs range with repetition rates of tens of kHz. Under special circumstances (*low charge* mode) the pulse length can be ≤ 10 fs [41].

HHG sources currently present many limitations: as like as laser plasma sources, high power lasers and/or very short pulses (close to transform limit) are required, a demand that often limits the repetition rate and lowers the averaged photon flux. Furthermore, all harmonics are generated in the same pulse making it difficult to select a specific wavelength and to filter out-of-band radiation, unless a diffraction grating is used (a solution hardly feasible for it suppresses the photon flux).

It is also impossible to produce circularly polarized harmonics [34] in inert gases[2]. The physical explanation of this effect is that when the freed electron is driven by circularly polarized radiation its trajectory never re-encounters the parent ion. In fact at the instant the electron is ionized its time-of-birth on the orthogonal polarization is shifted by $\pi/2$ with respect to the actual polarization (such is the phase difference between two orthogonal polarizations to produce circularly polarized light) and the trajectory on this direction is drifted away from the ion.

On the other hand radiation produced with these sources under suitable experimental conditions can have excellent spatial [43] and temporal coherence, being able for instance to synthesize the shortest light pulses ever [33], down in the attosecond regime. Also, the EUV and SXR pulses are naturally synchronized with the laser ones, which are available as *pump* pulses in a time-resolved experiment since they propagate collinearly with their harmonics. Last but not least HHG sources are low cost when compared to FELs and they are very compact ("tabletop").

In the following chapter the experimental setup is presented.

[2]They can be produced, however, in molecules with more sophisticated experimental setups as in [42].

Chapter 4

Experimental apparatus

4.1 The LASER source

The light source is a commercially available device from Coherent Inc.™ made up of multiple stages capable of producing 50 fs short laser pulses with average energy per pulse of 2.3 mJ at a repetition rate (R.R.) of 1 kHz in the spectral region of the near infrared. These stages are briefly described.

The first stage takes place in the Mira oscillator. In this device ultrashort gaussian shaped laser pulses at a R.R. of 76 MHz and at a wavelength tunable between 760 nm and 850 nm are synthesized by means of a Sapphire crystal doped with Titanium (Ti:Sapphire) from a continuous wave (CW) frequency doubled Nd:YAG pump laser (Verdi-5), which works at a wavelength of 532 nm and output power of 5 W. Such a broad band tunability in wavelength is assured by a birefringent filter installed in the cavity, which on the other hand temporally broadens the pulses.

The oscillator is generally operated at a central wavelength of 796 nm with a bandwidth of $\simeq$44 nm, generating nearly transform limited pulses of $\simeq$ 25 fs. The output power is usually $\simeq$ 350 mW.

The second stage takes place in the Legend regenerative amplifier. In this stage the low energy laser pulses exiting the oscillator are amplified to the average energy per pulse of 2.3 mJ and duration of 50 fs. The central wavelength is shifted to about 798 nm and the bandwidth, narrower, is approximately equal to 25 nm so that the output

pulses are only close to be transform limited.

The amplification scheme, called *"chirped pulse amplification"*, relies on another Ti:Sapphire crystal placed in an optical cavity. The crystal is seeded by the infrared pulses, which have been previously stretched by a pair of gratings, and is pumped by a frequency doubled $Nd : YLF_4$ pulsed Q-switched laser at a R.R. of 1 KHz. The amplification gain is proportional to the number of round trips the pulses travel in the cavity and is controlled by two Pockels cells [44]. The amplified pulses are then temporally compressed by another pair of gratings.

4.2 The coherent ultrashort EUV source

The laser wavelength is converted into its odd harmonics by means of the previously introduced process of High order Harmonic Generation (HHG). The harmonics can extend into the Extreme Ultra-Violet (EUV) region of the electromagnetic spectrum with features depending on the various experimental conditions.

The optical setup is showed in Fig. 4.1. It is composed of two separable vacuum chambers: in the first (Generation Chamber, or GC) the laser beam is focused in a cylindrical cell filled with Ne and the EUV radiation is produced; in the second a diffractive grating and an exit slit compose the monochromator.

The focusing of the laser in the cell occurs via a spherical mirror with focal length of 30 cm in order to achieve a low beam divergence after the focus.

The cell, with a diameter of 10 mm and length of 3 mm, is mounted on a moving stage and is sealed with a thin aluminum sheet. The intensity at the focus is strong enough to make a hole in both sheets allowing the gas to interact with the laser. Gas pressure is assured by a gas line piped to the cell and can be controlled from the outside with a micrometric valve.

Particular care is given to the materials of the mirrors (silver) and the thickness of the entrance window (only 0.5 mm) in order to preserve the pulse temporal structure.

The quality of the EUV radiation (intensity, monochromaticity and eventual energy shift of the harmonics) depends on phase matching requirements [45] and is controlled via the gas pressure and the cell position.

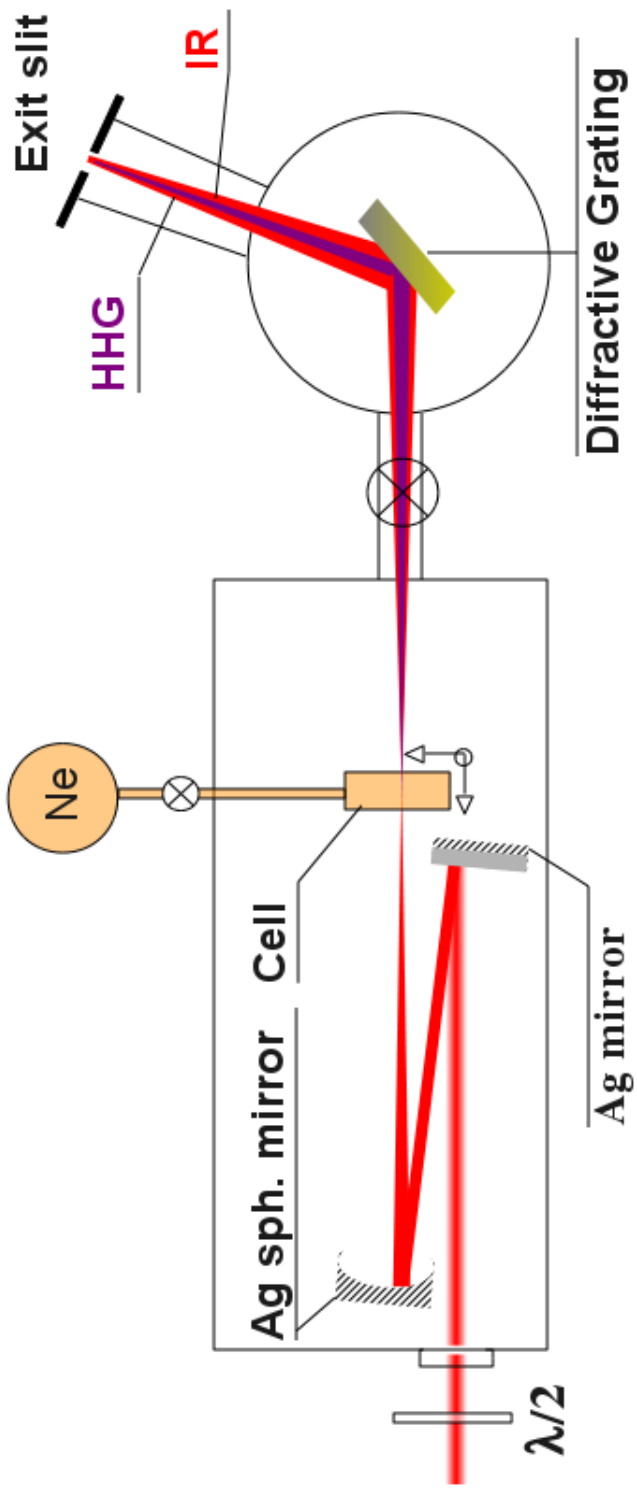


Figure 4.1: HHG experimental setup. The incoming laser beam is focused in the gas cell with a Ag spherical mirror. The harmonics produced co-propagates with the fundamental radiation in the monochromator chamber. Here a spherical diffractive grating can be operated either at its 1st order of diffraction, allowing a characterization of the HHG source, or at the 0th order (as in figure), reflecting either the harmonics and the fundamental. This last geometry allows to use the reflected fundamental as a *pump* beam in the time resolved experiment. The outgoing radiation is focused on an exit slit.

The IR beam and the EUV radiation propagate collinearly in the monochromator, equipped with a diffraction grating and an exit slit placed at a fixed distance from it.

The grating has a spherical curvature with radius of 1 m and the surface has a blaze profile with line density of 576 mm^{-1}. It is gold coated to enhance reflectivity at the EUV wavelengths. The nominal resolution is about 0.1 nm at 45 nm and its position is controlled via computer. The focusing of the EUV spectral plane on the slit prevents moving the latter while scanning the grating [45]. This can be operated at the 1st order of diffraction to select a desired harmonic, hence cutting the IR radiation (the *pump* in the time-resolved measurements), or it can be operated at the zero-th order of diffraction (using it as a mirror) to keep the IR pulse together with the EUV radiation (the *probe*). Spectral filtering of the latter is then performed with the aforementioned multilayer optics in the experimental chamber.

Control on the near-infrared linear polarization is achieved by means of a $\lambda/2$ plate placed before the generation chamber.

4.3 The TR-EUV/MLD experimental chamber

The radiation exiting the monochromator enters the experimental chamber (called "Magneto-Optical Anisotropy ANAlyser", M.O.A.A.N.A), which was designed and assembled to perform time-resolved magnetic dichroism with the HHG source.

The sample under study is a 30 nm thin film of Permalloy ($Ni_{80}Fe_{20}$) deposited on a Si substrate. The surface is perfectly flat as imaged with a Scanning Electron Microscope (SEM). The high magnetic permeability, the practically null magnetocristalline anisotropy and magnetostriction of the sample make it particularly suited to simplify these measurements.

The conceptual sketch of the geometry of the experiment is illustrated in Fig. 4.2.

When operating the monochromator at the zero-th order of diffraction the incoming IR radiation (the *pump* beam) is focused on the sample by a Au-coated doughnut shaped spherical mirror, while the EUV *probe* beam is focused by a multilayer (ML) spherical mirror. The properties of the latter assure good suppression of neighboring

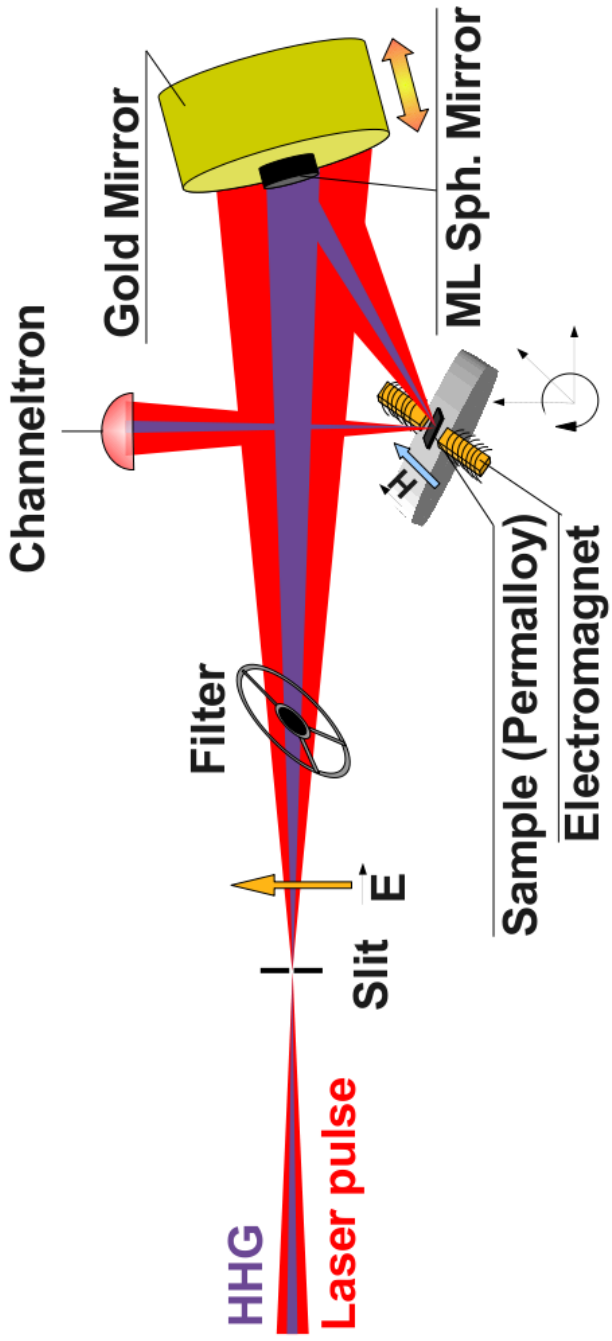


Figure 4.2: Experimental chamber setup. With linearly polarized radiation, a magnetic dichroism is obtained with the magnetic field transverse to the reflection plane and with p polarized radiation (as shown).

harmonics, as shown in Fig. 5.2. Both mirrors work close to normal incidence (see Tab. 4.1).

The waist radius of the focuses was measured by knife-edge technique and is approximately 150 µm.

The ML mirror is mounted on a moving stage, controlled via computer, which tunes the temporal delay between the *pump* and the *probe* pulses. Its position is checked by means of an LVDT transducer which has a linear response in the range of the displacements requested. The minimum controllable time delay allowed by this device is limited to $\simeq 5$ fs.

Spatial and temporal superposition close to the focal point (on the sample) is checked performing an autocorrelation with the second harmonic generation (SHG) from the IR laser light reflected from both mirrors in a BBO crystal that substitutes the sample.

To suppress eventual out-of-band radiation an *ad-hoc* filter is centered on the EUV beam path, as shown in the Fig. 4.2. To transmit the harmonic at ≈ 66 eV (Ni edge) a Zr plate of 60 nm or 150 nm is employed, since it has a steep decrease in the transmissivity for energies right above this edge. For the harmonic at ≈ 54 eV (Fe edge) an Aluminum plate of 400 nm is available.

Being these filters metallic, no IR radiation is transmitted in the EUV propagation cone. However, the remaining IR beam is allowed to propagate around the filter. This solution allows to spatially separate the *pump* and the *probe* beams, improving the spectral quality of the *probe* and limiting the fluence of the *pump* at the same time. Furthermore, it prevents heating of the ML mirror under the action of the IR radiation.

When operating the monochromator on the 1st order of diffraction, only a selected EUV radiation is allowed to propagate and the filter becomes inessential.

The sample is mounted on a manipulator with 4 degrees of freedom (3 translations and 1 rotation around the axis of the manipulator) and placed in the narrow gap of a home-made electromagnet capable of generating a magnetic field of $\simeq$100 gauss with 1 A continuous current. The electromagnet has been calibrated with a Hall probe gaussimeter showing that the hysteresis cycles have a remanence of 6 gauss and a coercive current of 400 mA.

The incidence angle of the beams is fixed close to 40° from normal (near the Brewster angle) and the electromagnet can be mounted transverse or longitudinal to the plane of reflection. The geometry should assure a high linear magnetic dichroism, as reported in [22, 24].

The reflected EUV radiation is detected by a channeltron (CEM), which is insensitive to the IR radiation (the quantum efficiency is different from zero only for energies $\gtrsim 7.5$ eV). The bias drop at the output of the CEM is preamplified by a factor of 100 and then detected by an oscilloscope and a computer.

GC Mirror focal length	300 mm
GC operating pressure (Ne)	$\approx 2 \times 10^{-3}$ mbar
Monochromator operating pressure	$\simeq 10^{-7}$ mbar
MOAANA operating pressure (vacuum)	$\simeq 6 \times 10^{-6}$ mbar
Zr filter thickness	60 or 150 nm
Al-filter thickness	400 nm
PPM reflectivity at $M_{2,3}$ Fe-edge (54 eV)	0.34
PPM reflectivity at $M_{2,3}$ Ni-edge (66 eV)	0.26
Sample reflectivity at M edges (working angle)	$\leq 3\%$
Photons per pulse (source)	$\approx 10^7$
Photons per pulse (on sample)	$\approx 10^3$
Photons per pulse (on detector)	≈ 10
PPM subtended angle	10°
Incident angle on the sample (from normal)	$\simeq 40°$
Sample thickness ($Fe_{20}Ni_{80}$)	30 nm
Maximum H field used	$\simeq 80$ gauss

Table 4.1: Main experimental parameters of the TR-EUV/MLD experimental setup. Adapted from [45]

Chapter 5

Multilayer Optics

In this chapter the optical devices used to manipulate the EUV/SXR radiation generated by the HHG process are presented. After a brief description of their working principles, it is given a detailed characterization of the mirrors employed in the experiment. At the end of the chapter it is introduced a clever way of implementing the same physical principles to change the state of polarization of this light.

5.1 Theory of multilayer optics

The peculiar behaviour of the EUV radiation interaction with materials, when compared to X-rays, allows great challenges for the optical manipulation of this kind of light.

The index of refraction can be written as [46]:

$$n(\omega) = 1 - \delta(\omega) + i\beta(\omega) = 1 - \frac{n_a r_e \lambda^2}{2\pi}\left(f_1^0(\omega) - i f_2^0(\omega)\right)$$

where n_a is the atomic density, $r_e = e^2/4\pi\epsilon_0 m_e c^2$ ($\simeq 2.82 \times 10^{-13}$ cm) is the classical electron radius and $f_1^0(\omega)$ and $f_2^0(\omega)$ are respectively the real and imaginary part of the scattering factor. The absorption cross-section of the material is directly related to the imaginary part, by [46]:

$$\sigma_{abs} = 2 r_e \lambda f_2^0(\omega)$$

while the reflection at normal incidence in the EUV and X-ray region can be approximated by [46]:

$$R_{\perp} = \frac{\delta^2 + \beta^2}{4}$$

In the optical region it is possible to work with refractive lenses at normal incidence because of the large availability of transparent materials. In the X-ray region, instead, it is possible to achieve total external reflection working at grazing incidence because the real part of the index of refraction is less than 1, i.e. the real part of the refractive index of air or vacuum [47].

In the middle region of the spectrum, the EUV region, it is not possible to use either these techniques because f_1^0 becomes close to 1 (even in the presence of the large fluctuations near the M absorption edges), meaning that it is impossible either to fabricate refractive lenses at normal incidence or to work at grazing incidence, since the acceptance angle would become very narrow[1] [46, 48].

It is possible, though, to work with diffractive optics, such as Fresnel zone plates, which are indeed widely used. Two drawbacks limit the adoption of this solution: chromatic aberrations and, mainly, poor efficiency [48].

Another solution is available that uses reflective optics. Single surface reflection, at normal incidence, suffers from low reflectivity for the same reason that lenses cannot be used.

However there's a clever way to improve the efficiency: multilayer coatings.

These optics are made by depositing alternating layers of two materials (or three [48]) of different refractive index over a substrate to form an interference coating (Fig. 5.1) . The layers are largely amorphous or, to some degree, polycrystalline, allowing deposition on curved surfaces, an interesting property that makes these optics suitable for imaging applications like in microscopes and telescopes [48]. Each pair of layers is referred to as "bilayer". At each bilayer interface reflection occurs. To reflect an incident wave of wavelength λ at normal incidence the d spacing between the bilayers is fixed to match $\lambda/2$ in order to have a coherent superposition of all the reflected waves. The behaviour can be explained in terms of the Bragg diffraction law. For

[1] The critical angle is approximated by $\theta_C = \sqrt{2\delta} = \sqrt{(n_a r_e \lambda^2 f_1^0)/\pi}$ [46], so when $f_1^0 \approx Z$ there is a wide angular interval for which total reflection would occur (the acceptance angle). On the contrary, when $f_1^0 \approx 1$ the interval becomes narrower.



Figure 5.1: Cross section TEM of a Molybdenum/Silicon (Mo/Si) multilayer. (From [48])

off-normal incidence[2]:

$$m\lambda = 2d\sin\theta$$

where m is the order of diffraction and θ is the grazing incident angle.

It is not difficult to imagine how challenging it is to deposit layers of the order of some nanometers to form a stable and well defined pattern. Two types of material are mostly used: a low Z material and a high Z material. The low Z material is chosen to have an absorption edge just above the desired wavelength in order to have a small β and a low δ (or even negative). This layer behaves almost transparent acting just like a "*spacer*". The second material is high Z to provide the highest difference in δ with respect to the "*spacer*", keeping absorption (β) low. Other physical and technological limitations also affect the choice of the materials [48]. Among these are the ability of the selected materials to form sharp and stable interfaces, their ability to be fabricated and their stability to time, temperature, working environment and oxidation.

It is also possible to adjust and estimate the bandwidth of the reflected light by choosing the number N of bilayers. In fact for a radiation with bandwidth $\Delta\lambda$ it is possible to define the "coherence length" as [46]:

$$l_{coh} = \frac{\lambda^2}{2\Delta\lambda}$$

[2]This formula can be corrected to account for the small refraction in the bilayer [46].

The coherence length gives the distance after which the different frequencies gets dephased to some degree. The physical request of a coherent superposition of the reflected waves from the topmost layer and deepest layer imposes that the thickness Nd of the stack must approximate the coherence length, that is [48]:

$$Nd \approx l_{coh} \quad \Rightarrow \quad \Delta\lambda \propto N^{-1}$$

5.2 Characterization of multilayer spherical mirrors

Multilayer coatings are successfully fabricated by different techniques [46]. Those employed in the present experiment were realized by Direct Current (DC) Magnetron Sputtering[3] at the Center for X-Ray Optics (CXRO) of the Lawrence Berkeley National Laboratory, Berkeley, by the group led by Prof. David Attwood.

They constitute two sets of spherical mirrors: one set is designed to reflect the 35th harmonic (at 22.8 nm) and the other the 43rd (at 18.8 nm) harmonic of a laser radiation centered at 800 nm, which corresponds to the $M_{2,3}$ absorption edges respectively of Fe at $\simeq 53$ eV and Ni at $\simeq 66$ eV. Resonant absorption should be assured by the width of these resonances which is close to 2 eV.

The spacer is constituted of Al, since its M edge at 72.5 eV makes it enough transparent, while the second layer is made of Zr, for its known surface compatibility with Aluminum [48]. A capping layer of SiO_2 protects the mirrors from oxidation.

In order to gain high reflectivity and suppression of undesired neighboring harmonics, these optics were produced with $N = 50$ bilayers of $d = 11.8$ nm for the Fe mirrors and $d = 9.6$ nm for the Ni mirrors. They are operated at almost normal incidence, as reported in Tab. 4.1.

The optical components have been tested at the beamline 6.3.2 of the Advanced Light Source (Berkeley) and subsequently with the HHG source located at the T-Rex laboratory at Elettra. This allowed to extend the characterization to lower order harmonics (until the 11th), an energy range not accessible at the ALS BL 6.3.2.

Fig. 5.2 shows the spectra obtained after reflection from a mirror and the sample. In the top part the spectra for the Fe (red) and Ni (blue) edge in the *cut-off* region

[3]For an exhaustive description of the process please refer to [48]

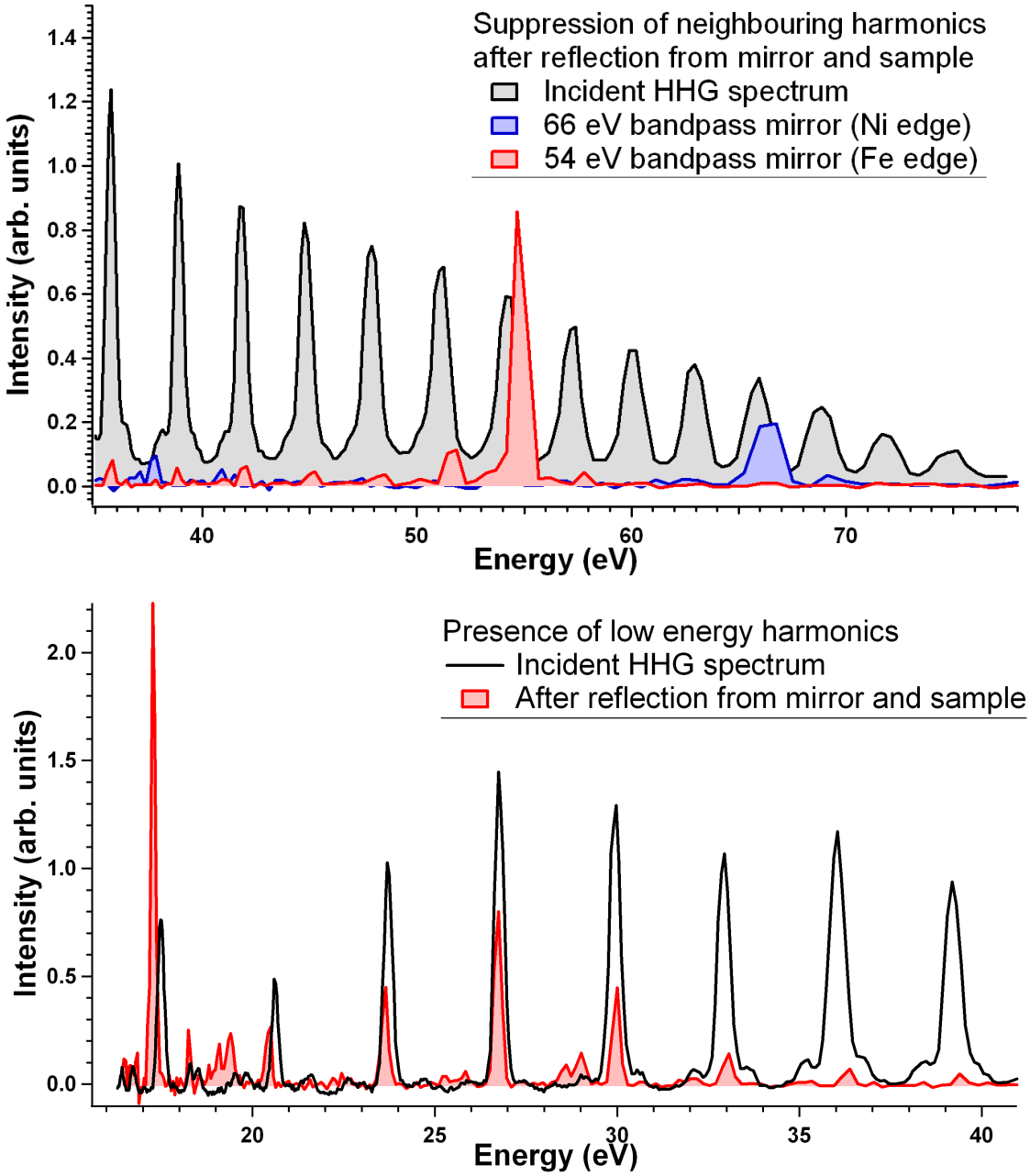


Figure 5.2: Comparisons between HHG spectra before and after reflection off the multilayer (ML) spherical mirrors for the M edges of Fe and Ni. (top) In the cut-off region harmonics close to the desired energy are well suppressed. (bottom) Low energy harmonics are more difficult to filter and more effort is needed.

are compared with the incident HHG spectrum, while in the bottom part a typical spectrum in the perturbative/plateau region is reported.

The measured reflectivity at the desired harmonics reaches a value of 30% for the Ni-edge mirror and almost 40% for the Fe-edge mirror, with a bandwidth of about 2 eV for the former and 3 eV for the latter.

They assure an optimum suppression of neighboring harmonics, while more effort is needed to filter low energy harmonics. In particular harmonics from the 7th (9.7 eV) to the 21st (32.6 eV) might be detected, with the latter and the 17th (26.3 eV) corresponding to the second order of diffraction from the mirror of the Fe and the Ni edges respectively. This low energy radiation incident on the detector is one of the major obstacles to time-resolved measurements, as extensively explained in chapter 6.2.

A shift of the reflected resonant harmonic to higher energies can be due to phase matching effects, as reported in [45]. The shift is also expected in damaging the mirrors, for these layers are known to shrink when heated (the d-spacing shortens). This can happen if they are shone with the "residual" infrared radiation that propagates collinearly with the harmonics. This effect could also explain the shift observed in the spectra. Other processes that can occur under heating are the inter-diffusion of the layers and the consumption of the SiO_2 capping layer, that results in an improved reflectivity of undesired harmonics, i.e. the mirrors act like a homogeneous Al-Zr interface. Hence extreme care has to be taken when dealing with these multilayer optics.

5.3 Obtaining circular polarization with multilayers

As already stated in chapter 3.2, circularly polarized EUV/SXR radiation cannot be produced by means of the HHG process for the intrinsic nature of the propagation step. In brief, when the electron is driven by elliptically polarized laser radiation, it acquires a transverse momentum component that eventually prevents re-collision with the parent ion.

In the optical region of the electromagnetic spectrum it is possible to switch from linear to circular polarization by means of so called "Quarter-Wave Plates" (QWP). These devices take advantage of their birefringent properties to induce a phase shift between the two polarization components that propagate in the crystal. Under suitable conditions the phase shift can be equal to $\pi/2$, resulting in circularly polarized outgoing light.

In the EUV or X-Ray region no materials are known to present these anisotropic properties.

It is possible, however, to switch from linearly polarized generated harmonics to circularly polarized ones by propagation through a suitable optical device. These devices take advantage of the different phase shift that s- and p- polarized light suffer when propagating through a multilayer plate set at the Brewster angle. Detailed description of their working principles can be found in [48]. These devices are referred to as Multi-Layered Quarter Wave Plates (ML-QWP).

As like as the mirrors, two sets of ML-QWP were designed for the experiment: one for radiation centered at ≈ 54 eV (Fe edge) and the other for ≈ 66 eV (Ni edge). A complete characterization of these devices is given in [45].

Although they are not employed in this thesis work, they will be used in the near future in order to perform magnetic circular dichroism (EUV-MCD). This will allow to disentangle the spin and orbital angular momenta, giving a clear description of the demagnetization procedure for the first time with an HHG source.

Chapter 6

Experimental data

In the first section of this chapter static data of magnetic dichroism on both the Fe and Ni $M_{2,3}$ absorption edges is presented. After recording a magnetic dichroic signal under reversal of the applied magnetic field, full hysteresis loops are acquired in the absence of the *pump* pulse with linearly polarized light. In the second section it is given a detailed explanation of the main issues that need to be addressed to pursue the time-resolved part of the experiment and possible solutions are reviewed.

6.1 Static data

Complete information on the sample magnetization, as explained in chapter 2.2, is obtained in general by analyzing both the intensity and the polarization of the reflected light. However, if the magnetization direction is transverse to the plane of reflection the polarization is not altered upon changing the magnetic field and only a reflectivity variation is expected. This configuration, which is called Transverse MOKE (T-MOKE), has been set up for the following measurements since it is best suited for the available detection system. Furthermore, only p polarized radiation is affected, i.e. no reflectivity variation should be expected with s polarized light. Also, the T-MOKE effect is linear in the magnetization meaning the measurements are sensitive to magnetization reversal and full hysteresis loops can be recorded.

At this step of the experiment the grating is operated at the 1st order of diffraction in order to cut the undesired IR radiation. The harmonics resonant with the sample

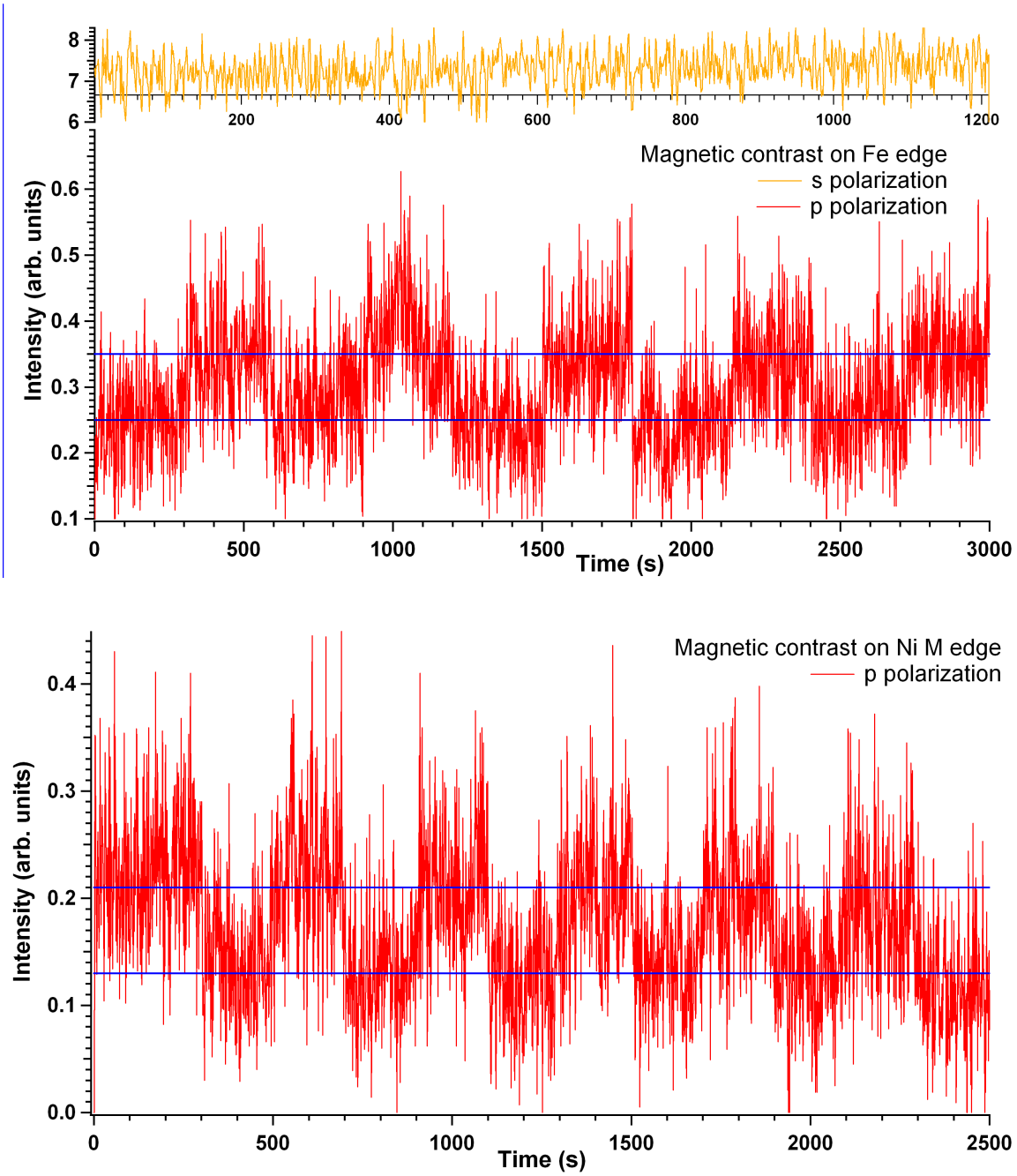


Figure 6.1: Linear magnetic contrast in T-MOKE geometry at the Fe (top) and Ni (bottom) M absorption edges. With p polarized light asymmetry parameters of 17% and 23% are obtained respectively. No dichroism is recorded with s polarized light, proving its magnetic origin. Blue lines show the average signals with two anti-parallel orientations of the applied magnetic field, which intensity is 60 gauss.

M absorption edges are selected by the monochromator (either the 35th or the 43rd harmonics).

As a first test only the presence of EUV magnetic dichroism at the hysteresis tails was checked. The data is reported in Fig. 6.1 for both the Fe and Ni edges. It shows the detected signal as a function of time, while switching the orientation of the applied magnetic field H, whose intensity was set at 60 gauss. With p polarized light the reflectivity of the sample enhances when H = - 60 gauss and lowers when H = + 60 gauss. The same effect is absent when s polarized light is employed (inset in the top graph), demonstrating its magnetic origin.

The strength of the T-MOKE signal is commonly quantified in terms of the *asymmetry parameter* [23]:

$$A = \frac{I_+ - I_-}{I_+ + I_-}$$

where I_+ and I_- are the reflected intensities for two anti-parallel orientations of the magnetization. Asymmetries of 17% and 23% are obtained respectively for Fe and Ni, much higher than reported in [2], at the fixed incident angle of $\simeq$40° from normal. However, asymmetries as high as 73% have been recorded close to the $M_{2,3}$ edge of Fe in T-MOKE geometry at an angle of incidence of 45° [24]. Determination of the index of refraction of the magnetized sample by reflectivity and ellipsometric analysis show that the dichroic signal is highly enhanced right on the absorption edges [49].

Subsequently, full hysteresis loops were acquired. These are shown in Fig. 6.2 on a relative asymmetry scale for visual clarity. The same data on an absolute intensity scale is reported in the insets. The one on the Fe edge was acquired soon after the previous measurements and indeed the asymmetry parameter in this case is $\simeq$ 13%, very close to what reported above. On the contrary, different experimental conditions could be at the origin of the non-reproducibility of high asymmetry on the Ni edge. In fact an asymmetry of only $\simeq$ 5% could be obtained in this case.

As reported in [22, 24], T-MOKE signals are strongly dependent on the angle of incidence when compared to dichroic measurements with circularly polarized light. In particular the highest T-MOKE asymmetries are expected in a narrow interval centered at $\simeq$ 45° (the Brewster angle of the sample), while they decrease by a factor $\gtrsim$ 4 for angles $\lesssim$ 40°.

This strong behaviour implies that small changes in the experiment geometry can hide most of the dichroism, as could have happened for the Ni hysteresis. In the future complete control on the angle by moving the detector together with the sample may be helpful.

The coercive field for Fe can be estimated $\simeq 10$ gauss, matching what measured in [2].

On the other hand, the reversal of the magnetization is not as sharp as in [2] probably indicating the presence of impurities where motion of domain walls gets stuck [50]. Reflectivity measurements close to an absorption edge are surface sensitive techniques due to the short penetration length of radiation in matter, only few tens of nanometers. Hence oxidation of the surface, which is expected due to the bad vacuum conditions and the absence of cleaning tools, can contaminate the hysteresis, smoothing the magnetization reversal.

As can be inferred from the traces of Fig. 6.1, the measurements are affected by an extremely low "signal/noise" ratio, where as "signal" it is meant the variation in the reflectivity under changes in the magnetization[1].

Each point is usually averaged over $256 \div 512$ laser pulses, but still a very low frequency noise component persists. This imply extremely long acquisition times: each hysteresis of Fig. 6.2 is actually averaged over 250 loops, each loop taking about 50 seconds, for a total duration of about 3 hours and 30 minutes. Signal stability over such a long temporal window is not assured at all and a reference signal is desirable.

One source of low frequency noise can be laser instabilities, either in intensity or in pulse shape. These fluctuations are less than 5% of the IR signal, but can be enhanced by the extreme non-linear nature of the HHG process. However, an accurate analysis on the correlation between these two signals in necessary.

Other contributions to noise can come from fluctuations in gas pressure in the cell, or shot-noise. Shot-noise is due to the intrinsic statistical fluctuations on the number of detected photons and is typical of low intensity sources. Increasing the signal lowers

[1] Changes in the magnetization are not thought just as switches of orientation, that lead to the highest possible reflectivity variation, but could also be magnitude variations like those performed to record hysteresis loops or induced by a *pump* pulse. These situations demand even higher "signal/noise" ratios (tougher bounds).

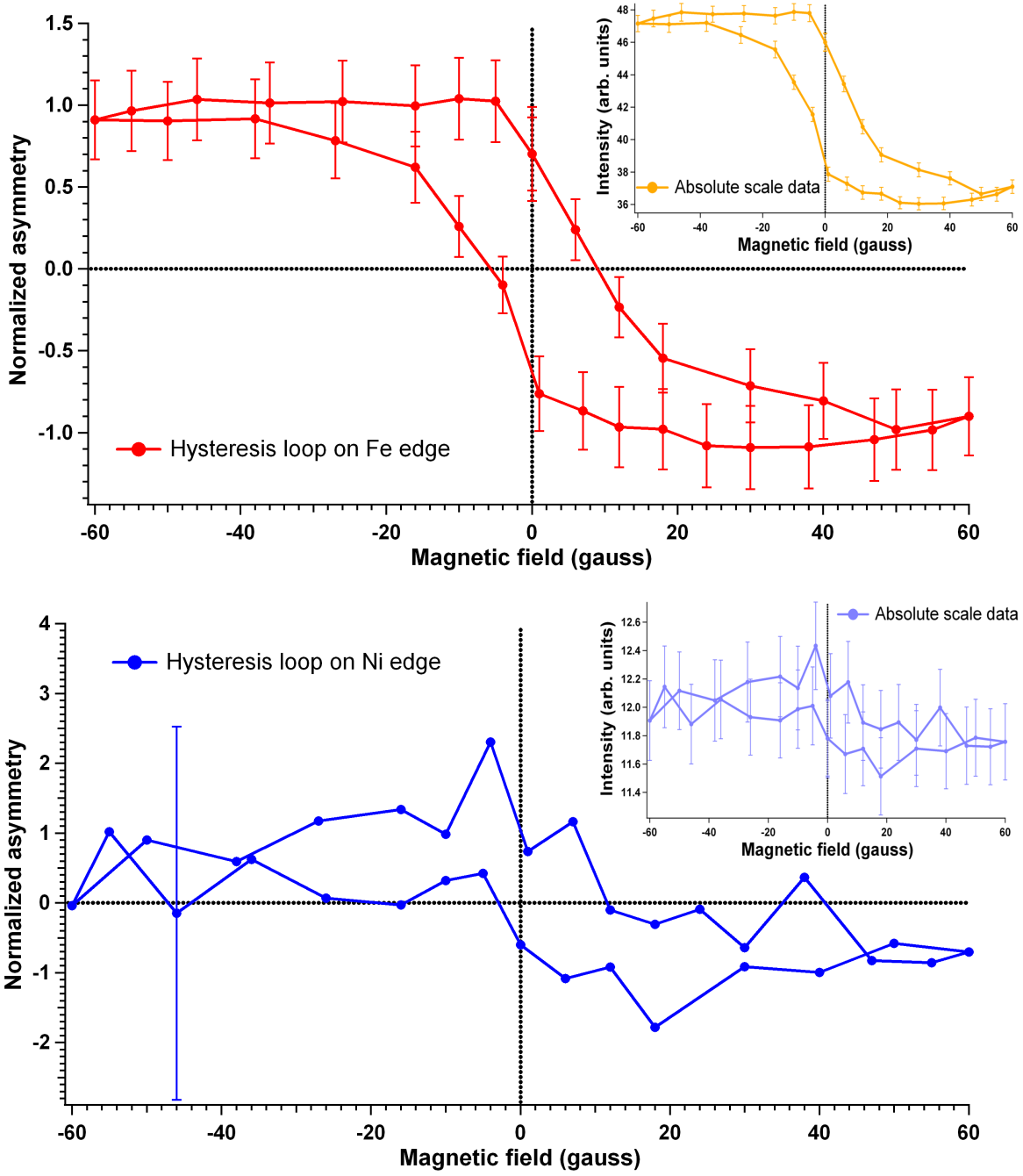


Figure 6.2: Hysteresis loops acquired at the Fe (top) and Ni (bottom) M absorption edges. The main graphs are plotted on a relative scale (asymmetry), while those on an absolute scale are shown in the insets.

the "signal/noise" ratio because while the numerator is proportional to N (the average number of photons), the denominator grows only as $\sqrt{N}$. Another positive consequence of increasing the signal is that the asymmetry also increases. Significant effort was put in increasing the intensity of the High Harmonic source and one solution is presented in the next section.

6.2 Towards ultrafast demagnetization dynamics

In order to perform time-resolved measurements the grating must be operated at the zero-th order of diffraction to allow the *pump* pulse to propagate in the chamber.

Obviously all High Harmonics are allowed too.

The current detection system of the absolute reflected intensity is sensitive to out-of-band radiation, i.e. undesired harmonics that are reflected by the ML mirror and the sample, which are indeed present as already shown in Fig. 5.2. This represents a main issue since the dichroic signal, already small by itself, is further suppressed below noise level by the superposition with this fluctuating signal that doesn't show any magnetic asymmetry.

As a matter of fact, acquisition of hysteresis loops with the grating operated at the zero-th order of diffraction has not succeeded yet.

Some possible "easy" solutions are under study.

The conceptually easiest one is to filter out-of-band harmonics by propagation of the beam through a suitable material, like Zr. This material was chosen for its steep decrease in transmissivity at energies $\lesssim 65$ eV (see Fig. 6.3, left graph). Although transmissivity at the Ni edge is hardly higher than 50%, harmonics below the 11th and above the 19th should be suppressed to a good extend. Unfortunately transmissivity reaches 23% for harmonics between the 13th and the 17th, but preliminary data is encouraging, showing a good suppression on the whole spectral range.

For the same reasons this material could not be suited for Fe edge, for which Al can be tried as it presents higher transmissivity at 54 eV (see right graph of Fig. 6.3). On the other hand, this metal has an almost flat response at lower energies and may not filter properly out-of-band radiation.

The employment of filters has major drawbacks on photon flux, which is already

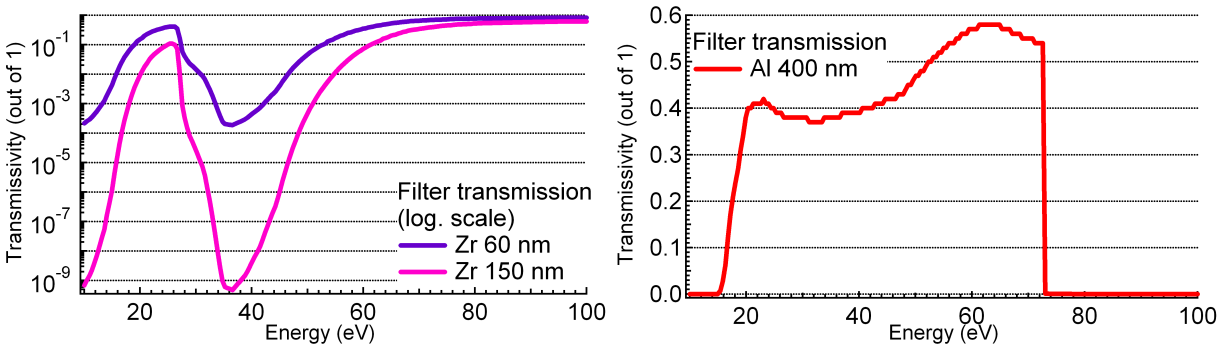


Figure 6.3: Transmissivities of filters employed or suggested for the experiment. (left) Two Zr films of 60 nm and 150 nm are compared (logarithmic scale), (right) A film of 400 nm of Al (linear scale). (From [47])

extremely low. A compromise must then be found between flux and spectral quality of the EUV radiation. For this reason very thin films of these materials, only 60 nm or 150 nm of Zr and 400 nm of Al, have been deposited on a 3 mm diameter ring, as pictured in Fig. 4.2. The results are encouraging but some work has still to be done to recover a decent dichroic signal.

Another solution that can be employed is HHG with pulses as short as $\simeq 10$ fs.

Pulse compression can be achieved by propagation of the focused laser beam in a hollow fiber filled with Ne gas [51, 52]. The typical fiber length is close to 1 m and the gas pressure is $\simeq 2$ bar. In the first place the spectrum is broadened in the range $650 \div 900$ nm by the interaction of the pulses with the gas (the process is referred to as "*self-phase modulation*"), while in the second place the spectral dispersion induced by propagation in the fiber and in the gas is compensated by reflection off six *chirped* mirrors. The output pulses are then temporally compressed with respect to the input pulses in virtue of the broader spectrum.

Fig. 6.4 shows the High Harmonic spectrum generated in Ne with such short laser pulses: the *cut-off* region broadens into a continuum and the photon flux increases by a factor $\approx 2 \div 4$ (depending on other experimental parameters); the *plateau* and the perturbative regions, instead, tend to be suppressed. Because of this combined effect, pulse compression can be a promising tool to increase the "signal/noise" ratio acting both on the numerator and the denominator.

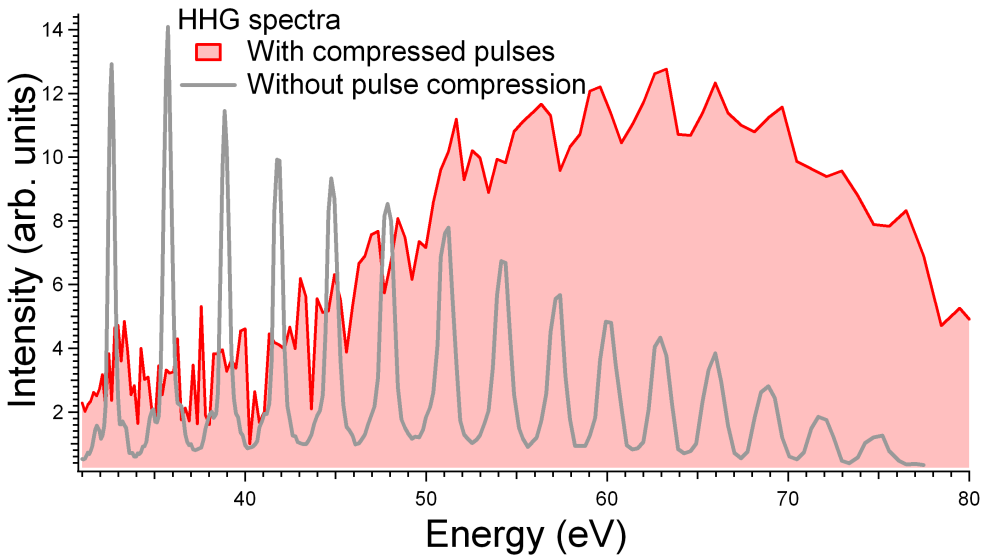


Figure 6.4: Comparison between HHG spectra obtained with (red) $\simeq$ 10 fs and $\simeq$ 0.9 mJ laser pulses and (blue) $\simeq$ 60 fs and $\simeq$ 2.2 mJ laser pulses. The spectra refer to photons detected right after the monochromator, before reflection off the ML mirror. Since they were acquired is different experimental conditions, a rigorous comparison on the photon flux is not allowed.

The matter of out-of-band radiation can be addressed also by dispersing the various wavelengths after the sample by simply moving the grating to intercept the reflected beam. Although monitoring just a selected harmonic would be enough, detection of the full spectrum by means of a MicroChannel Plate (MCP) or a EUV-CCD camera would provide an excellent reference signal at the same time. In fact, what matters is the change in the integrated intensity at a given photon energy (normalized to the total number of photons) when switching the magnetic field.

Almost the same advantages can be achieved by moving from detection of photons to detection of photoelectrons emitted by the sample, by means of a Time-Of-Flight (TOF) electron spectrometer. Even though implementation of this detection system is not as easy as photon detection (think for example of the extreme sensitivity of electrons trajectories to magnetic fields), photoemission experiments allow a straightforward determination of the energy bands in the sample, an appealing feature to easy picture the dynamics of spin-up and spin-down electrons. On the other hand reflectivity measurements are easy to implement but the physics involved is hidden behind the complex nature of the index of refraction. Last but not least, photoelectron detection

can be best suited to the low flux of an HHG source, where *space charge* effects must be avoided[2].

Once recovered a good static dichroic signal, the *pump-probe* experiment can present some more issues linked to the collinear geometry of the two beams. If on one hand it simplifies the search for spatial and temporal coincidence, on the other hand it limits the possibility of controlling the two pulses independently. It is mandatory, for instance, to limit the fluence of the *pump* to just few mJ/cm^2 in order not to damage the sample.

It may be also necessary to implement an acquisition scheme more sensitive to small variations in the magnetic asymmetry, by using for example a lock-in amplifier. This geometry, however, makes very difficult to "chop" the *probe* without affecting the *pump*. A transverse geometry could be rather preferred, with the *pump* pulse derived from a portion of the full laser beam before it enters the Generation Chamber. This allows full control of the pumping process, on the other hand making alignment more difficult.

In conclusion, although some "easy" to implement promising solutions have been presented, a conceptual restyle of the detection and acquisition scheme might be necessary in the near future if the former methods turn out to be inefficient.

[2]Space charge effects arise when the photoelectron bunch in highly populated and coulomb repulsion within the bunch results in distorted spectra. This condition in frequently met with laser sources, where the pulse time structure is sharp when compared to synchrotron sources. Low intensity lasers with high repetition rates must be employed, in order to avoid these effects while keeping a good statistics.

Conclusions

In this work full hysteresis loops at the $M_{2,3}$ absorption edges of Fe and Ni metals were acquired in an independent way, taking advantage of the elemental sensitivity of the absorption process. Linearly polarized photons delivered by a HHG source were employed, making of this work the second experiment of its kind. Higher magnetic contrasts were achieved when compared to the first published work, but still in accordance with other measurements reported in the literature.

As explained in the text, the acquired data is affected by an extremely low signal/noise ratio. A low frequency noise component is present, that implies acquisition periods as long as hours. Since stability over such a long interval is not assured, in the future the use of a reference signal is desirable.

Some hypothesis about the origin of this noise are proposed, like instabilities in the laser system or in the gas pressure, but due to the low photon flux incident on the sample and on the detector the best candidate could be *shot-noise*. In this sense, future work should aim at increasing the efficiency of the HHG process, a severe limitation of these sources that prevents their adoption as good alternatives to other EUV/SXR light sources.

The acquisition of the static hysteresis with a monochromatized source represented the first step towards time-resolved studies on ultrafast demagnetization phenomena.

The second step is the acquisition of the same measurements with the broad spectrum provided by the EUV source. The generated radiation is then no longer monochromatized with the diffraction grating, but with the multilayer optical devices made *ad-hoc* for the experiment.

A spectral characterization of these devices allowes to point the presence of out-of-band radiation at lower energies than the absorption edges, together with the present detection system, as main obstacles to the complete success of the experiment.

Some possible techniques to get rid of this radiation were tested. Spectral filtering can be obtained, for example, by means of very thin plates of Zr or Al placed in the path of the beam. Although the preliminary results show a good suppression of low energy harmonics, the already low photon flux is unavoidably affected by the absorption properties of these materials.

As explained in the text, a clever way to solve the problem can be the generation of High order Harmonics by means of compressed ($\simeq$ 10 fs) laser pulses. In this regime a simultaneous suppression of harmonics in the perturbative and plateau regions and an enhanced intensity in the cut-off were observed. This method has clearly two major advantages: besides naturally quenching out-of-band radiation, it will increase the signal/noise ratio easing data acquisition.

Some alternative options on the detection system are also reviewed, that could solve these problems at once and pave the way towards a *pump-probe* experiment.

In fact the ability to perform a spectral analysis after reflection from the sample will completely rule out the problem of unwanted detection of out-of-band radiation. For example, implementation of a diffractive grating between the sample and the detector would do the task. Furthermore, substitution of the present detector with a MicroChannel Plate (MCP) or a CCD camera will also allow a correct normalization of the desired signal to the total recorded intensity, helping the acquisition process.

Switching to photoelectron detection, rather than photon detection, could be another valid alternative. Detection with a Time-Of-Flight (TOF) spectrometer, for instance, also provides a direct measurement on the band structure and can be best suited for low photon flux sources, provided the repetition rate is high.

In conclusion, further work and implementation of some of the presented improvements will allow to probe ultrafast demagnetization dynamics with the HHG source for the second time ever.

Switching to circularly polarized EUV radiation will allow to disentangle the rapid evolution of spin and orbital angular momentum, providing such information on the M edges for the first time. Besides, the availability of circularly polarized HHG sources

may be of great interest for many other applications, providing a low-cost alternative to FELs and *slicing* beamlines.

Appendix A

Derivation of reflection coefficients for T-MOKE

The origin of magneto-optical effects is a different propagation of electromagnetic waves in a material depending on its polarization. Hence it is mandatory to find the refractive index of such waves in order to predict their behaviour. This is done from the Maxwell equations in a medium:

$$\begin{aligned} \vec{\nabla} \cdot \vec{D} &= \rho_{free} \\ \vec{\nabla} \times \vec{E} &= -\frac{\partial \vec{B}}{\partial t} \\ \vec{\nabla} \cdot \vec{B} &= 0 \\ \vec{\nabla} \cdot \vec{H} &= \mu_0 \vec{J}_{free} + \mu_0 \frac{\partial \vec{D}}{\partial t} \end{aligned}$$

and the linear constitutive relations (valid in homogeneous and linear media)

$$\begin{aligned} \vec{D} &= \overleftrightarrow{\epsilon} \vec{E} = \epsilon_0 \vec{E} + \vec{P} \\ \vec{H} &= \overleftrightarrow{\mu} \vec{B} = \vec{B} - \mu_0 \vec{M} \\ \vec{J}_{free} &= \overleftrightarrow{\sigma} \vec{E} \end{aligned}$$

The wave equation can be obtained taking the curl of the second equation:

$$\begin{aligned} \vec{\nabla} \times \vec{\nabla} \times \vec{E} &= -\frac{\partial}{\partial t} \vec{\nabla} \times \vec{B} \\ \vec{\nabla} \left(\vec{\nabla} \cdot \vec{E} \right) - \nabla^2 \vec{E} &= -\frac{1}{c^2} \frac{\partial^2 \vec{E}}{\partial t^2} - \frac{1}{c^2} \frac{\partial^2 \vec{P}}{\partial t^2} - \mu_0 \frac{\partial \vec{J}_{free}}{\partial t} \end{aligned}$$

where it is put $\mu = 1$. As explained in [20] this doesn't mean that magnetic materials cannot be accounted for, but rather that the electric response of the medium dominates the wave propagation. By imposing propagation of a plane monochromatic wave as

$$\vec{E}(\vec{r},t) = \vec{E}_0 e^{i(\vec{k}\cdot\vec{r}-\omega t)} = \vec{E}_0 e^{i(\omega\vec{n}\cdot\vec{r}/c-\omega t)}$$

the wave equation can be rewritten as [20]:

$$\frac{\omega^2}{c^2}\left[-\overleftrightarrow{n:n} + n^2\overleftrightarrow{1} - \overleftrightarrow{\epsilon} - i\frac{\overleftrightarrow{\sigma}}{\omega\epsilon_0}\right]\cdot\vec{E} = 0$$

where $\overleftrightarrow{n:n_{ij}} = n_i n_j$ is known as the *dyadic product.* Renaming $\overleftrightarrow{\epsilon} = \overleftrightarrow{1} + \overleftrightarrow{\epsilon} + i\overleftrightarrow{\sigma}/\omega\epsilon_0$ one has:

$$\frac{\omega^2}{c^2}\left[n^2\overleftrightarrow{1} - \overleftrightarrow{n:n} - \overleftrightarrow{\epsilon}\right]\cdot\vec{E} = 0$$

which is also referred to as the Fresnel equation. The eigenvalues and the eigenvectors of the above equation correspond respectively to the refractive indexes along three crystal axes and the normal modes of propagation along those axes. Once given the dielectric tensor, the refractive index and the associated eigenwaves can be obtained respectively solving [20]:

$$\mathrm{Det}\left[n^2\overleftrightarrow{1} - \overleftrightarrow{n:n} - \overleftrightarrow{\epsilon}\right] = 0 \qquad \text{(A.1)}$$

$$\left[n^2\overleftrightarrow{1} - \overleftrightarrow{n:n} - \overleftrightarrow{\epsilon}\right]\cdot\vec{E} = 0 \qquad \text{(A.2)}$$

The dielectric tensor of a magnetized medium has a form related to the crystal symmetry and the direction of the magnetization with respect to crystal axes. For simplicity it is considered a crystal with cubic symmetry. In the case of no net magnetic moment the refractive index is isotropic and the dielectric tensor is diagonal. However when the material gets magnetized it assumes the form [20, 53]:

$$\overleftrightarrow{\epsilon} = \begin{pmatrix} \epsilon_\perp & iQ\epsilon_\perp & 0 \\ -iQ\epsilon_\perp & \epsilon_\perp & 0 \\ 0 & 0 & \epsilon_\parallel \end{pmatrix}$$

where $\parallel$ and $\perp$ refer to the magnetization direction. By symmetry considerations, Q is odd under inversion of the magnetization [25, 20]:

$$Q(-M,\omega) = -Q(M,\omega)$$

Assuming this is along x and the reflection plane is transverse to it (lying in the yz plane), the refractive index can be decomposed as $\vec{n} = n\sin\theta\hat{y} - n\cos\theta\hat{z} = n_y\hat{y} + n_z\hat{z}$. Here $\sin\theta$ and $\cos\theta$ are in general complex quantities derived from application of Snell's law at the surface. The Fresnel equation becomes:

$$\begin{pmatrix} n^2-\epsilon_\parallel & 0 & 0 \\ 0 & n^2-n_y^2-\epsilon_\perp & -n_yn_z+iQ\epsilon_\perp \\ 0 & -n_yn_z-iQ\epsilon_\perp & n^2-n_z^2-\epsilon_\perp \end{pmatrix} \cdot \begin{pmatrix} E_x \\ E_y \\ E_z \end{pmatrix} = 0$$

Condition A.1 gives the following refractive indexes [53, 20]:

$$n_s^2 = \epsilon_\parallel; \qquad n_p^2 = \epsilon_\perp(1-Q^2)$$

Solving for the respective modes through equation A.2 it is found that the first refractive index is related to s-polarized waves propagating in the material. Thus, no coupling with the magnetization occurs in this case. On the other hand, p-polarized waves are the modes consistent with the second solution, provided that [53]:

$$E_z = -\frac{\sin^2\theta}{n^2\sin\theta\cos\theta - iQ}E_y$$

Calculation of the reflection coefficients requires matching the boundary conditions at the surface, i.e. continuity of the parallel components of the electric and magnetic fields. In the following E^i and E^r are the incidence and reflected electric fields. Calling ϕ the incident angle from the normal to the surface ($\hat{z}$), it is possible to find the reflected field by solving [53]:

$$\begin{aligned} E^i\cos\phi + E_y - E^r\cos\phi &= 0 \qquad (E_y \text{ continous}) \\ E^r + \frac{n_p}{\cos\theta}\left[1 + iQ\frac{\sin\theta}{\cos\theta}\right]E_y + E^i = 0 &\qquad (H_x \text{ continous}) \end{aligned}$$

where it is assumed that the incident and reflected waves are propagating in vacuum. Finally, the reflection coefficient has the form [53]:

$$\tilde{r}_{pp} = \frac{E^r}{E^i} = \frac{n_p \cos\phi \left[1 + iQ(\sin\theta/\cos\theta)\right] - \cos\theta}{n_p \cos\phi \left[1 + iQ(\sin\theta/\cos\theta)\right] + \cos\theta}$$

After some calculations, it is possible to separate the magnetic contribution Δ_{pp} by the usual non-magnetic reflection coefficients [54]:

$$\widetilde{r}_{pp} = r_{pp} + \Delta_{pp} = \frac{n_p \cos\phi - \cos\theta}{n_p \cos\phi + \cos\theta} + i\frac{2n_p \cos\phi \sin\theta Q}{(n_p \cos\phi + \cos\theta)^2}$$

Thus the T-MOKE effect is odd in the magnetization, for it is directly related to the off-diagonal part of the dielectric tensor. Similar calculations can be performed for all MOKE geometries and other Magneto-Optical effects [20, 53].

List of Figures

1.1 Areal density of commercial storage devices versus the year they came on the market. 9

1.2 Time - energy correlation line given by $t = h/E$. The typical energetic ranges of magnetic interactions are also shown. (From [6]) 12

1.3 Experimental result of Beaurepaire. The trace is proportional to the sample magnetization. Soon after the *pump* pulse excites the system, the magnetization drops, evidencing a $\simeq 2$ ps demagnetization dynamics. (From [1]) 14

1.4 Representation of the ultrafast demagnetization process. A femtosecond laser pulse interacts *coherently* with charges and spins of electrons, which subsequently thermalize and interact together with the lattice (*incoherent* evolution). The relative weight of the deexcitation channels and the nature of the relaxation process is highly debated. The demagnetization is also found to emit THz photons [17]. (From [15]) 16

2.1 The XMCD effect at the $L_{2,3}$ edges of Fe. (right) XAS spectra obtained with circular polarization at different magnetization orientations (showed as arrows in the colored boxes). (left) Pictorial representation of the spin-dependent absorption process. The core states are assumed spin-orbit split, while the valence band is spin-split (From [6]). 20

2.2 Three different geometries for the Kerr effect: (a) Polar geometry or P-MOKE, (b) Longitudinal geometry or L-MOKE and (c) Transverse geometry or T-MOKE. (From [20]) 23

3.1 HHG spectra generated in Argon and Neon using $\simeq 2.2$ mJ, $\simeq 50$ fs, near-IR ($\lambda_0 \simeq$ 800 nm) laser pulses. For Argon the perturbative, plateau and cut-off regions are highlighted. Due to the higher ionization potential I_p of Neon, its cut-off region extends to higher energy but the total number of photons is lower (this spectrum is multiplied by a factor of 10 in order to make a visual comparison with Argon). The 35th and the 43rd harmonics, employed in this thesis work, are resonant with respectively the Fe and Ni M-absorption edges. 28

3.2 Pictorial representation of the HHG process. (a) the atomic coulomb barrier is lowered by the superposition with the oscillating laser field (yellow) allowing the electron leaving the atom by tunnel effect (ionization); (b) the same electron is driven away from the parent ion by the field and when this reverses (c) the electron is pulled back eventually colliding with the parent atom (d) while high order non-linear emission of photons can occur. (From [33]) 29

3.3 Illustration of the re-collision process: when the bound state electron wavefunction Ψ_g (a) is superimposed to the continuum wavepacket Ψ_c (b, that shows the real part) a dipole is induced (c), represented by an asymmetric charge density distribution. The induced dipole oscillates back and forth as the continuum wavepacket propagates, leading to emission of harmonics. (From [31]) 31

3.4 Processes that compete with the harmonic emission during the re-collision step. (From [40]) 32

3.5 Comparison of present coherent EUV/SXR sources. On the left are plotted the regions of photon energy/wavelength and pulse duration that they cover. Ultrafast sources occupy the region not spanned by either synchrotrons or usual lasers. The dashed line represent the single-cycle limit. HHG sources can be very ductile and can produce pulses that are closest to this limit. (From [38]). On the right the average brilliance of these sources is shown. The most brilliant are FELs presently under construction, which have high peak brilliance and high repetition rate. HHG sources mainly suffer the low repetition rate, as explained in the text. (From [38]) 33

4.1 HHG experimental setup. The incoming laser beam is focused in the gas cell with a Ag spherical mirror. The harmonics produced co-propagates with the fundamental radiation in the monochromator chamber. Here a spherical diffractive grating can be operated either at its 1st order of diffraction, allowing a characterization of the HHG source, or at the 0th order (as in figure), reflecting either the harmonics and the fundamental. This last geometry allows to use the reflected fundamental as a *pump* beam in the time resolved experiment. The outgoing radiation is focused on an exit slit. 39

4.2 Experimental chamber setup. With linearly polarized radiation, a magnetic dichroism is obtained with the magnetic field transverse to the reflection plane and with p polarized radiation (as shown). 41

5.1 Cross section TEM of a Molybdenum/Silicon (Mo/Si) multilayer. (From [48]) . . . 47

5.2 Comparisons between HHG spectra before and after reflection off the multilayer (ML) spherical mirrors for the M edges of Fe and Ni. (top) In the cut-off region harmonics close to the desired energy are well suppressed. (bottom) Low energy harmonics are more difficult to filter and more effort is needed. 49

6.1 Linear magnetic contrast in T-MOKE geometry at the Fe (top) and Ni (bottom) M absorption edges. With p polarized light asymmetry parameters of 17% and 23% are obtained respectively. No dichroism is recorded with s polarized light, proving its magnetic origin. Blue lines show the average signals with two anti-parallel orientations of the applied magnetic field, which intensity is 60 gauss. 54

6.2 Hysteresis loops acquired at the Fe (top) and Ni (bottom) M absorption edges. The main graphs are plotted on a relative scale (asymmetry), while those on an absolute scale are shown in the insets. 57

6.3 Transmissivities of filters employed or suggested for the experiment. (left) Two Zr films of 60 nm and 150 nm are compared (logarithmic scale), (right) A film of 400 nm of Al (linear scale). (From [47]) 59

6.4 Comparison between HHG spectra obtained with (red) $\simeq$ 10 fs and $\simeq$ 0.9 mJ laser pulses and (blue) $\simeq$ 60 fs and $\simeq$ 2.2 mJ laser pulses. The spectra refer to photons detected right after the monochromator, before reflection off the ML mirror. Since they were acquired is different experimental conditions, a rigorous comparison on the photon flux is not allowed. 60

List of Acronyms

2TM	Two Temperature Model
3TM	Three Temperature Model
as	attosecond
CCD	Charge-Coupled Device
CEM	Channeltron Electron Multiplier
CW	Continuous Wave
CXRO	Center for X-Ray Optics
EUV	Extreme Ultra-Violet
FEL	Free Electron Laser
fs	femtosecond
FWHM	Full Width at Half Maximum
GC	Generation Chamber
GMR	Giant Magneto-Resistance
HHG	High order Harmonic Generation
IR	InfraRed
LBNL	Lawrence Berkeley National Laboratory
MCD	Magnetic Circular Dichroism
MCP	Micro-Channel Plate
ML	MultiLayer
MLD	Magnetic Linear Dichroism
MOAANA	Magneto-Optical Anisotropy ANAlizer
MOKE	Magneto-Optical Kerr Effect
PPM	Pump-Probe Mirror
ps	picosecond
QWP	Quarter-Wave Plate
R.R.	Repetition Rate
SASE	Self-Amplified Spontaneous Emission
SHG	Second Harmonic Generation
SXR	Soft X-Rays
T-Rex, TR	Time Resolved
TOF	Time-Of-Flight electron spectrometer
XAS	X-ray Absorption Spectroscopy

List of Symbols

$\vec{B}$	Magnetic induction
$\vec{H}$	Magnetic intensity
$\vec{E}$	Electric field
$\vec{\sigma}$	Spin operator
$\vec{\boldsymbol{m}}$	Magnetic moment
$\vec{\mathbf{L}_{\mathbf{ph}}}$	Photon angular momentum
r_T	Reflection matrix in T-MOKE
$R_{\pm}$	Reflectivity for antiparallel magnetic field orientations
r_{pp}	Fresnel diagonal reflection coefficient for p-polarized light
Δ_{pp}	Magnetic contribution to r_{pp}
γ	Keldysh's parameter
ω_0	Laser central frequency
λ_0	Laser central wavelength
τ_T	Tunneling time
T_{osc}	Laser central frequency period
I_p	First ioniziation potential
E_0	Central frequency peak electric field
$\hbar$	Planck constant $/2\pi$
$\vec{\mathbf{d}}(t)$	Dipole matrix element
$n(\omega)$	Complex refractive index
$\delta(\omega)$	Contribution to the real part of $n(\omega)$
$\beta(\omega)$	Imaginary part of $n(\omega)$
$f_1^0(\omega)$	Contrib. to real part of the atomic scattering factor
$f_2^0(\omega)$	Imaginary part of the atomic scattering factor
n_a	Atomic density
r_e	Classical electron radius
σ_{abs}	Absorption cross-section
θ_c	Total external reflection critical angle
Z	Atomic number
d	bilayer spacing in ML structures
l_{coh}	Coherence length
A	Asymmetry parameter

Bibliography

[1] E. Beaurepaire, J.-C. Merle, A. Daunois, and J.-Y. Bigot, *Ultrafast spin dynamics in ferromagnetic Nickel*, Physical Review Letters **76** (1996), no. 22, 4250.

[2] Chan La-O-Vorakiat, Mark Siemens, Margaret M. Murnane, Henry C. Kapteyn, Patrik Grychtol, Roman Adam, Claus M. Schneider, Justin M. Shaw, Hans Nembach, and T. J. Silva, *Ultrafast demagnetization dynamics at the M edges of magnetic elements observed using a tabletop high-harmonic soft x-ray source*, Physical Review Letters **103** (2009), no. 25, 257402.

[3] C Stamm, T Kachel, N Pontius, R Mitzner, T Quast, K Holldack, S Khan, C Lupulescu, E F Aziz, M Wietstruk, H A Dürr, and W Eberhardt, *Femtosecond modification of electron localization and transfer of angular momentum in nickel.*, Nat Mater **6** (2007), no. 10, 740–3.

[4] C. Stamm, N. Pontius, T. Kachel, M. Wietstruk, and H. A. Durr, *Femtosecond x-ray absorption spectroscopy of spin and orbital angular momentum in photoexcited Ni films during ultrafast demagnetization*, Physical Review B **81** (2010), 104425.

[5] P. Fisher, *lecture on "nanoscale magnetic imaging" at uc berkeley. http://www.youtube.com/watch?v=m3ahf-hdhw8.*

[6] J. Stöhr and H. C. Siegmann, *Magnetism - from fundamentals to nanoscale dynamics.*

[7] M. van Kampen, C. Jozsa, J. Kohlhepp, P. LeClair, L. Lagae, W. de Jonge, and B. Koopmans, *All-optical probe of coherent spin waves*, Physical Review Letters **88** (2002), no. 22, 227201.

[8] J.Y. Bigot et al., *Ultrafast phenomena xiii*, Chemical Physics, Berlin, 2002.

[9] A V Kimel, A Kirilyuk, P A Usachev, R V Pisarev, A M Balbashov, and Th Rasing, *Ultrafast non-thermal control of magnetization by instantaneous photomagnetic pulses.*, Nature **435** (2005), no. 7042, 655–7.

[10] M. Agranat et al., *Interaction of picosecond laser pulses with the electron, spin and phonon subsystem of nickel*, Sov. Phys. JETP, 59:804 (1984).

[11] A. Vaterlaus, T. Beutler, and F. Meier, *Spin-lattice relaxation time of ferromagnetic gadolinium determined with time-resolved spin-polarized photoemission*, Physical Review Letters **67** (1991), no. 23, 3314.

[12] A. Vaterlaus, T. Beutler, D. Guarisco, M. Lutz, and F. Meier, *Spin-lattice relaxation in ferromagnets studied by time-resolved spin-polarized photoemission*, Physical Review B **46** (1992), no. 9, 5280.

[13] J. Hohlfeld, E. Matthias, R. Knorren, and K. Bennemann, *Nonequilibrium magnetization dynamics of nickel*, Physical Review Letters **78** (1997), no. 25, 4861.

[14] A. Scholl, L. Baumgarten, R. Jacquemin, and W. Eberhardt, *Ultrafast spin dynamics of ferromagnetic thin films observed by fs spin-resolved two-photon photoemission*, Physical Review Letters **79** (1997), no. 25, 5146.

[15] Jean-Yves Bigot, Mircea Vomir, and Eric Beaurepaire, *Coherent ultrafast magnetism induced by femtosecond laser pulses*, Nature Physics **5** (2009), no. 7, 515.

[16] I.E. Radu, *Ultrafast electron, lattice and spin dynamics on rare-earth metal surfaces*, Ph.D. thesis, 2006.

[17] E. Beaurepaire, G. M. Turner, S. M. Harrel, M. C. Beard, J.-Y. Bigot, and C. A. Schmuttenmaer, *Coherent terahertz emission from ferromagnetic films excited by femtosecond laser pulses*, Applied Physics Letters **84** (2004), no. 18, 3465.

[18] B Koopmans, G Malinowski, F Dalla Longa, D Steiauf, M Fähnle, T Roth, M Cinchetti, and M Aeschlimann, *Explaining the paradoxical diversity of ultrafast laser-induced demagnetization.*, Nat Mater **9** (2010), no. 3, 259–65.

[19] G. Zhang and W. Hübner, *Laser-induced ultrafast demagnetization in ferromagnetic metals*, Physical Review Letters **85** (2000), no. 14, 3025.

[20] P. M. Oppeneer, *Handbook on magnetic materials*, vol. 13.

[21] C. Gutt, L.-M. Stadler, S. Streit-Nierobisch, A. Mancuso, A. Schropp, B. Pfau, C. Günther, R. Könnecke, J. Gulden, B. Reime, J. Feldhaus, E. Weckert, I. Vartanyants, O. Hellwig, F. Staier, R. Barth, M. Grunze, A. Rosenhahn, D. Stickler, H. Stillrich, R. Frömter, H. Oepen, M. Martins, T. Nisius, T. Wilhein, B. Faatz, N. Guerassimova, K. Honkavaara, V. Kocharyan, R. Treusch, E. Saldin, S. Schreiber, E. Schneidmiller, M. Yurkov, S. Eisebitt, and G. Grübel, *Resonant magnetic scattering with soft x-ray pulses from a free-electron laser operating at 1.59 nm*, Physical Review B **79** (2009), no. 21, 212406.

[22] Hartmut Ho*chst, Dennis Rioux, Dai Zhao, and David L. Huber, *Magnetic linear dichroism effects in reflection spectroscopy: A case study at the Fe $M_{2,3}$ edge*, Journal of Applied Physics **81** (1997), no. 11, 7584.

[23] H.-Ch. Mertins, D. Abramsohn, A. Gaupp, F. Schäfers, W. Gudat, O. Zaharko, H. Grimmer, and P. Oppeneer, *Resonant magnetic reflection coefficients at the Fe 2p edge obtained with linearly and circularly polarized soft x rays*, Physical Review B **66** (2002), no. 18, 184404.

[24] M HECKER, P OPPENEER, S VALENCIA, H MERTINS, and C SCHNEIDER, *Soft x-ray magnetic reflection spectroscopy at the 3p absorption edges of thin Fe films*, Journal of Electron Spectroscopy and Related Phenomena **144-147** (2005), 881.

[25] P. M. Oppeneer, *Slides from summer school schwerte 2007.*

[26] J. Hannon, G. Trammell, M. Blume, and Doon Gibbs, *X-ray resonance exchange scattering*, Physical Review Letters **61** (1988), no. 10, 1245.

[27] C.-C. Kao, C. Chen, E. Johnson, J. Hastings, H. Lin, G. Ho, G. Meigs, J.-M. Brot, S. Hulbert, Y. Idzerda, and C. Vettier, *Dichroic interference effects in circularly polarized soft-x-ray resonant magnetic scattering*, Physical Review B **50** (1994), no. 13, 9599.

[28] J. Geissler, E. Goering, M. Justen, F. Weigand, G. Schütz, J. Langer, D. Schmitz, H. Maletta, and R. Mattheis, *Pt magnetization profile in a Pt/Co bilayer studied by resonant magnetic x-ray reflectometry*, Physical Review B **65** (2001), no. 2, 020405.

[29] Zenghu Chang, Andy Rundquist, Haiwen Wang, Margaret Murnane, and Henry Kapteyn, *Generation of coherent soft x rays at 2.7 nm using high harmonics*, Physical Review Letters **79** (1997), no. 16, 2967.

[30] R. Velotta, N. Hay, M. B. Mason, M. Castillejo, and J. P. Marangos, *High-order harmonic generation in aligned molecules*, Physical Review Letters **87** (2001), no. 18, 183901.

[31] J Itatani, J Levesque, D Zeidler, Hiromichi Niikura, H Pépin, J C Kieffer, P B Corkum, and D M Villeneuve, *Tomographic imaging of molecular orbitals.*, Nature **432** (2004), no. 7019, 867–71.

[32] U. Teubner and P. Gibbon, *High-order harmonics from laser-irradiated plasma surfaces*, Reviews of Modern Physics **81** (2009), no. 2, 445.

[33] P. B. Corkum and Ferenc Krausz, *Attosecond science*, Nature Physics **3** (2007), no. 6, 381.

[34] P. B. Corkum, *Plasma perspective on strong field multiphoton ionization*, Phys. Rev. Lett. **71** (1993), no. 13, 1994–1997.

[35] M. Lewenstein, Ph. Balcou, M. Ivanov, Anne L'Huillier, and P. Corkum, *Theory of high-harmonic generation by low-frequency laser fields*, Physical Review A **49** (1994), no. 3, 2117.

[36] L. V. Keldysh, *Soviet. physics jept*, **47** (1964), no. 1495.

[37] M Uiberacker, Th Uphues, M Schultze, A J Verhoef, V Yakovlev, M F Kling, J Rauschenberger, N M Kabachnik, H Schröder, M Lezius, K L Kompa, H-G Muller, M J J Vrakking, S Hendel, U Kleineberg, U Heinzmann, M Drescher, and F Krausz, *Attosecond real-time observation of electron tunnelling in atoms.*, Nature **446** (2007), no. 7136, 627–32.

[38] T Pfeifer, C Spielmann, and G Gerber, *Femtosecond x-ray science*, Reports on Progress in Physics **69** (2006), no. 2, 443.

[39] G. Vampa, *Generation of light pulses in the extreme ultraviolet (30 - 60 nm) by means of ultrashort laser fields at 400 nm*, B.Sc. Thesis (2008).

[40] Ferenc Krausz, *Attosecond physics*, Reviews of Modern Physics **81** (2009), no. 1, 163.

[41] *http://lcls.slac.stanford.edu.*

[42] Olga Smirnova, Serguei Patchkovskii, Yann Mairesse, Nirit Dudovich, David Villeneuve, Paul Corkum, and Misha Ivanov, *Attosecond circular dichroism spectroscopy of polyatomic molecules*, Physical Review Letters **102** (2009), no. 6, 063601.

[43] Randy A. Bartels, Ariel Paul, Hans Green, Henry C. Kapteyn, Margaret M. Murnane, Sterling Backus, Ivan P. Christov, Yanwei Liu, David Attwood, and Chris Jacobsen, *Generation of spatially coherent light at extreme ultraviolet wavelengths*, Science **297** (2002), no. 5580, 376–378.

[44] G. R. Fowles, *Introduction to modern optics*, 2nd ed.

[45] Alberto Simoncig, *The role of electron recoiling mechanism in coherent light high-order harmonics generation: from the source to the applications*, Ph.D. thesis, Physics, 2010.

[46] D. Attwood, *Soft x-ray and extreme ultraviolet radiation, principles and applications*, 2000.

[47] *http://www-cxro.lbl.gov.*

[48] Andrew Lee Aquila, *Development of extreme ultraviolet and soft x-ray multilayer optics for scientific studies with femtosecond/attosecond sources*, Ph.D. thesis, 2009.

[49] S Valencia, A Gaupp, W Gudat, H-Ch Mertins, P M Oppeneer, D Abramsohn, and C M Schneider, *Faraday rotation spectra at shallow core levels: 3p edges of Fe, Co, and Ni*, New Journal of Physics **8** (2006), no. 10, 254.

[50] R. P. Feynman, *The feynman lectures on physics vol. 2, ch. 37, pag. 9.*

[51] W. R. Boyd, *Nonlinear optics*, 2nd ed.

[52] W. Rudolph J. C. Diels, *Ultrashort laser pulse phenomena*, 2nd ed.

[53] Robert P. Hunt, *Magneto-optic scattering from thin solid films*, Journal of Applied Physics **38** (1967), no. 4, 1652.

[54] Z. J. Yang and M. R. Scheinfein, *Combined three-axis surface magneto-optical kerr effects in the study of surface and ultrathin-film magnetism*, Journal of Applied Physics **74** (1993), no. 11, 6810.

Ringraziamenti

Sebbene il periodo di tesi non sia durato più di un nove mesi, questo lavoro rappresenta il frutto di sofferte decisioni che ho preferito affrontare a viso scoperto nell'arco degli ultimi due anni, per alcuni "troppo" severamente. Se queste scelte fossero o meno evitabili, non posso dirlo con certezza, e comunque ha ormai poca importanza. Delle molte persone conosciute durante gli ultimi sei anni, alcune meritano di essere citate per la loro incrollabile amicizia, o per avere condiviso dei sogni, o semplicemente per avere incrociato la mia via al momento giusto.

Non posso quindi non ringraziare il Prof. Parmigiani per l'ovvio contributo che ha fornito alla mia crescita professionale, e per il meno ovvio approccio comprensivo con il quale ha accettato e sostenuto importanti scelte di carattere personale. Il suo modo lungimirante ed ad ampio spettro di interpretare la Ricerca mi affascina, e il carattere delle sue lezioni costituisce a mio parere una buona sintesi tra rigore e senso fisico così difficile da rendere.

La maggior parte del merito di questo lavoro di tesi è dovuto, per ora, alla concezione innovativa di questo tipo di esperimento. Desidero ringraziare, quindi, colui che per primo si è cimentato in tale impresa e che mi ha dato la possibilità di partecipare: Alberto. Con la sua presenza e la sua guida puntuale avrei potuto sicuramente sfruttare di più questi mesi in laboratorio.

Desidero ringraziare Marco Malvestuto per le consulenze "gratuite" che hanno contribuito, a tratti in maniera pregnante, allo sviluppo dell'esperimento e alla disponibilità e simpatia dimostrata durante le misure su BACH.

Non potrò dimenticare, inoltre, il supporto scientifico e umano di Barbara, con la quale ho passato ore in tarda serata ad aspettare la formazione su uno schermo, punto per punto, di improbabili isteresi. Colgo l'occasione per scusarmi con Marco Zangrando se l'ho fatta arrivare tardi per cena. In lei ho scoperto una persona dotata

di immense doti umane, nonché un carattere che si incastra alla perfezione col mio (cosa non facile...). Gli istanti di ilarità pura che hanno caratterizzato alcuni momenti in laboratorio hanno reso estremamente piacevole la sua compagnia, così come quella degli altri membri del gruppo T-Rex: Cesare, Luigi (grazie per il software!), Giacomo, Federico, Goran e Michele.

Un grazie particolare al tecnico Gianluca Bortoletto, che ha perso ore preziose a creare i pezzi fondamentali che costituiscono la gloriosa camera MOAANA.

Per quanto riguarda lo sport, le parole non bastano per esprimere tutta la felicità che ho provato a fare parte di un gruppo così unito. Gli splendidi rapporti che conservo con la dirigenza, nonostante le mie scelte, con Ugo e con la squadra, dal capitano all'ultimo panchinaro, sono fonte di commozione nei momenti di riflessione. Di ognuno di loro conservo ricordi particolari, ma mai avrei sperato di conoscere una persona come Andrea Brazzatti: il suo carattere, la sua simpatia e la sua grinta costituiscono, per me, un modello da imitare.

Per quanto riguarda la sfera privata, desidero ringraziare gli amici di sempre: Mattia, Nico, Corra, Lucio e anche Jacopo. Nonostante i contatti siano poco frequenti, ci lega una storia di quasi vent'anni, e molti altri ne condivideremo. Non posso assolutamente scordare, inoltre, quelli che mi sono stati più vicini negli ultimi tempi, Marco in primis: se ci fossimo incontrati alle superiori sarebbe stato mitico. E la mia compagna, Agnese, la quale, tra l'altro, pazientemente custodisce ogni singolo pezzetto della mia memoria.

Per concludere desidero esprimere la mia riconoscenza ai parenti e in particolar modo ai miei genitori, ai quali è dedicata questa tesi. Potrei finalmente dire che mio padre ha trovato la *soluzione all'uomo in più*, forse perchè finalmente...

... è finita !